

Identifying Key Controls on Storm Formation over the Lake Victoria Basin

BETH J. WOODHAMS

University of Leeds, Leeds, United Kingdom

CATHRYN E. BIRCH

University of Leeds, Leeds, and Met Office, Exeter, United Kingdom

JOHN H. MARSHAM

University of Leeds, and National Centre for Atmospheric Science, Leeds, United Kingdom

TODD P. LANE

University of Melbourne, and ARC Centre of Excellence for Climate Extremes, Melbourne, Australia

CAROLINE L. BAIN AND STUART WEBSTER

Met Office, Exeter, United Kingdom

(Manuscript received 15 March 2019, in final form 20 June 2019)


ABSTRACT

The Lake Victoria region in East Africa is a hot spot for intense convective storms that are responsible for the deaths of thousands of fishermen each year. The processes responsible for the initiation, development, and propagation of the storms are poorly understood and forecast skill is limited. Key processes for the life cycle of two storms are investigated using Met Office Unified Model convection-permitting simulations with 1.5 km horizontal grid spacing. The two cases are analyzed alongside a simulation of a period with no storms to assess the roles of the lake–land breeze, downslope mountain winds, prevailing large-scale winds, and moisture availability. While seasonal changes in large-scale moisture availability play a key role in storm development, the lake–land-breeze circulation is a major control on the initiation location, timing, and propagation of convection. In the dry season, opposing offshore winds form a bulge of moist air above the lake surface overnight that extends from the surface to ~1.5 km and may trigger storms in high CAPE/low CIN environments. Such a feature has not been explicitly observed or modeled in previous literature. Storms over land on the preceding day are shown to alter the local atmospheric moisture and circulation to promote storm formation over the lake. The variety of initiation processes and differing characteristics of just two storms analyzed here show that the mean diurnal cycle over Lake Victoria alone is inadequate to fully understand storm formation. Knowledge of daily changes in local-scale moisture variability and circulations are keys for skillful forecasts over the lake.

1. Introduction

Lake Victoria, in tropical East Africa (Fig. 1), is a hot spot for intense convective storms and lightning (Flohn and Fraedrich 1966; Virts et al. 2013; Albrecht

et al. 2016). It is estimated that 30 million people live on the shores of Lake Victoria, of which ~3.5 million, including 200 000 fishermen, are dependent on the lake for their livelihoods (Semazzi 2011). Boating accidents, mainly associated with severe weather and dangerous water currents, are thought to cause 5000 deaths on the

 Denotes content that is immediately available upon publication as open access.

Corresponding author: Beth J. Woodhams, b.j.woodhams@leeds.ac.uk



This article is licensed under a [Creative Commons Attribution 4.0 license](http://creativecommons.org/licenses/by/4.0/) (<http://creativecommons.org/licenses/by/4.0/>).

DOI: 10.1175/MWR-D-19-0069.1

© 2019 American Meteorological Society

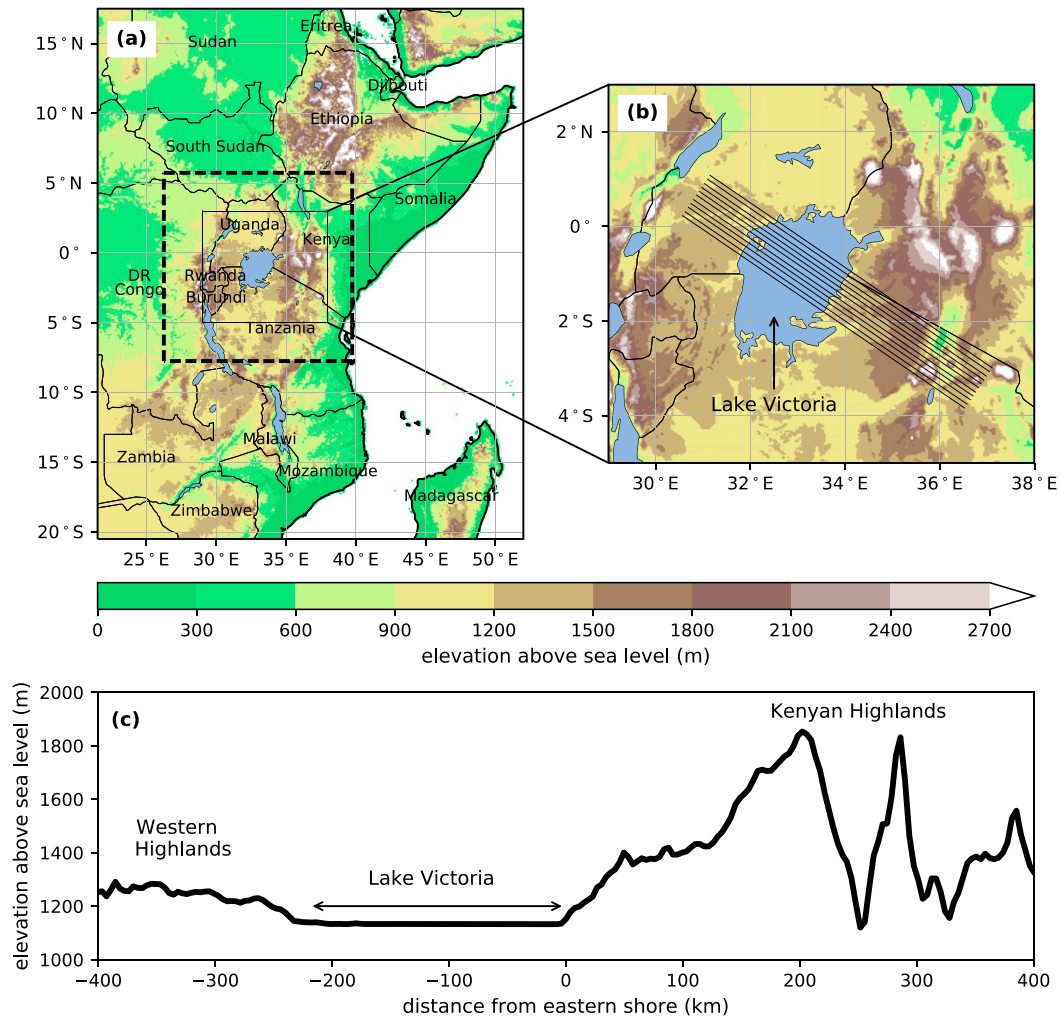


FIG. 1. (a) A map showing the orography over East Africa, covering the domain of the 4.4 km simulation. The dashed box encloses the 1.5 km domain. Elevation data are from the Global Land One-kilometer Base Elevation (GLOBE) Digital Elevation Model (Hastings and Dunbar 1999). (b) An enlarged section of the 1.5 km domain. Elevation data show the 1.5 km simulation input orography. The black lines show transects parallel to the eastern shore. (c) The mean 1.5 km simulation orography along the transects plotted in (b).

lake every year (Semazzi 2011; Cannon et al. 2014). Despite recent improvements in weather forecast products over East Africa, including the addition of convection-permitting (CP) modeling (Chamberlain et al. 2014; Woodhams et al. 2018), forecasting storms over Lake Victoria remains a major challenge. A basic process-based understanding of the initiation, development, and propagation of individual storms within the Lake Victoria basin region is lacking, as is an understanding of the factors impacting the intensity of the storms, in particular the rainfall and near-surface winds.

Due to Lake Victoria's position on the equator, prevailing winds are from the east over most of the troposphere, with some seasonal variability due to the

movement of the ITCZ (Flohn and Fraedrich 1966; Nicholson 1996). The frequency of storms over the lake is enhanced as the ITCZ moves north over the lake during March–May (known locally as the “long rains”) and returns south between October and December (the “short rains”), although storms occur throughout the year. Winds over the lake have a northerly component between November and March and southerly component between April and October, as the position of the ITCZ changes. Modeling studies have shown that most of the available moisture over the region is advected from the Indian Ocean by the prevailing easterly monsoonal winds, although much of this is blocked by the high ridge of mountains to the east of the lake (Mukabana and Pielke 1996; Anyah et al. 2006).

A regional diurnal circulation system, driven by temperature and moisture differences between the lake and land, locally modifies the large-scale wind pattern across Lake Victoria (Flohn and Fraedrich 1966). This circulation consists of a divergent lake breeze during the afternoon and convergent land breeze overnight, which have a control on convection and rainfall over the lake and surrounding catchment. Flohn and Burkhardt (1985) suggested that this circulation occurs on average 175 days yr^{-1} and is responsible for approximately half of the annual precipitation over the lake. Using observations from stations close to the lake shore, Datta (1981) showed the lake breeze to reach its maximum strength at 1500 LT (LT = UTC + 3 h), with rainfall over land occurring in the late afternoon. The land breeze was shown to be strongest between 0600 and 0900 LT, when rainfall is most frequent over the lake. There is a dependence of the strength of the lake–land-breeze circulation on the lake–land temperature contrast (Fraedrich 1972). While the temperature of the lake remains almost constant at around 25°C, the temperature of the air over land can vary between 15° and 30°C over the diurnal cycle (Lumb 1970).

The interaction of the lake and land breezes with the easterly prevailing winds causes an asymmetry in the spatial pattern of winds and rainfall over the lake (Datta 1981; Song et al. 2004). During the evening, the relatively cool and moist lake breeze across the eastern shore converges with the warm and relatively dry air from over the Kenyan Highlands, which is advected toward the lake by the prevailing winds. This convergence maximizes mean rainfall along the east coast between 1800 and 0100 LT, when rainfall is at a minimum over central and western parts of the lake. This minimum occurs due to two secondary effects highlighted in observations by Datta (1981) and Ba and Nicholson (1998) and in model simulations by Thiery et al. (2015). The first is associated with the release of latent heat from deep convection along the eastern shore that is advected westward in the prevailing wind and acts to stabilize the atmosphere over the lake. The second is the compensating subsidence over the lake produced by the return flow of the lake breeze, which occurs between 2000 and 5000 MSL.

The mean rainfall maximum over central and western parts of the lake occurs around 0800 LT and is attributed to convergence between the prevailing easterlies and the land breeze from the western shore during the morning (Datta 1981). Since the atmosphere cools overnight, but the lake surface temperature remains fairly constant, a steep lapse rate in the BL destabilizes the atmosphere over the lake, such that it is conducive to deep convection (Flohn and Burkhardt 1985; Datta 1981). While the

above understanding was developed using a limited number of gauge stations, the diurnal cycle of the spatial rainfall pattern was later verified by several studies using satellite data (Ba and Nicholson 1998; Yin et al. 2000; Nicholson and Yin 2002; Camberlin et al. 2018).

In addition to lake and land breezes, topography has been shown to play an important role in the diurnal cycle over the Lake Victoria basin (Lumb 1970; Okeyo 1986; Mukabana and Piekle 1996; Anyah et al. 2006). The lake sits on a plateau in the Great African Rift System at approximately 1100 m, surrounded by high orography to the west, and the particularly significant slopes of the Kenyan Highlands to the east (Fig. 1c). It is suggested that the highlands may encourage daytime upslope (anabatic) winds, which induce the lake-breeze front (and associated convergence and rainfall) farther inland. At night, downslope (katabatic) winds are expected; as cooler air is brought to the lake shore, a more intense land breeze is generated, with greater convergence and convection over the lake. Asymmetry in the spatial pattern of rainfall over the lake is enhanced, since the steeper mountains to the east encourage stronger katabatic flow, pushing the area of convergence farther west (Anyah et al. 2006).

Other lake-breeze circulations around the world have been studied via field campaigns and modeling. In particular, there is a wealth of research focused on Lake Michigan and the other Great Lakes in North America (Lyons 1972; Lyons and Olsson 1972; Keen and Lyons 1978; Sills et al. 2011). Relative to Lake Victoria, the frequency of lake–land-breeze circulation development is reduced in this region due to the strong influence of midlatitude weather systems. Discussion of land breezes is generally neglected in the literature, especially the interaction of two land breezes from opposite shores. However, the role of land-breeze convergence in the formation of Great Lake snowstorms has been shown by Passarelli and Braham (1981), Ballentine (1982), and Hjelmfelt and Braham (1983).

While many studies have looked at the effect of Lake Victoria on the mean diurnal cycle of storm activity (Mukabana and Piekle 1996; Song et al. 2004; Anyah et al. 2006; Thiery et al. 2015; Camberlin et al. 2018), the dynamical processes involved have not been studied in detail or at the individual storm level. This is due in part to a lack of observations—especially over the lake itself and at a high time and spatial resolution—as well as the requirement of very high-resolution modeling to capture the details of storm dynamics. Studies have shown that high-resolution CP modeling is vital for reproducing observed phenomena associated with sea breezes (Birch and Reeder 2013; Birch et al. 2014, 2015) and the same is likely applicable to lake breezes. In particular,

CP models have improved representation of cold pools (Marshall et al. 2013). Woodhams et al. (2018) and Finney et al. (2019) showed that CP MetUM simulations have an improved diurnal cycle in rainfall over East Africa relative to parameterized models, although Finney et al. (2019) showed that rainfall intensities can be too high over the lake.

This paper uses CP simulations with the Met Office Unified Model (MetUM) at high horizontal resolution (1.5 km grid spacing) to perform a process-based study of the initiation and propagation of two storms over the Lake Victoria basin. The existing literature described here tends to focus on the mean or composited diurnal cycle of circulation or storms, but lacks any detailed analysis of individual storm cases. Such studies have shown that large-scale moisture fluxes into the basin have a strong control on storm formation and that the lake–land–breeze circulation and orography play important roles in determining the mean diurnal cycle of convection. However, it is hypothesized that these different factors and their interactions will differ from the mean on daily time scales. This hypothesis is investigated by comparing case studies of a wet season and dry season storm to a third case study of a dry period over the lake (i.e., a “control” case, which illustrates the underlying lake–land–breeze circulation in dry conditions). This paper identifies the key controls on storm formation and shows that the mean diurnal cycle is insufficient to understand the processes responsible for individual storms due to a diverse range of conditions and triggers for storm initiation. It is noted that the three cases presented here are insufficient to fully represent the variety of processes leading to the formation of storms over the Lake Victoria basin. However, the chosen cases highlight a number of key factors that should be investigated going forward.

The model configuration for the simulations is described in section 2 and the case studies are introduced in section 3a. The dry period case study is used to describe the lake–land–breeze circulation in section 3b and the storm case studies are analyzed in sections 3c and 3d. Section 3e compares and contrasts all three cases. Schematics of the three cases and a comparison table are presented in section 4. The results are discussed and conclusions are drawn in section 5.

2. Methods

a. Model

The MetUM was used to perform the numerical simulations, with a configuration similar to that in Stratton et al. (2018), based on the Met Office UKV

regional model (Tang et al. 2013). The simulations consisted of a driving global model and two doubly one-way nested limited-area convection-permitting (CP) models, with horizontal grid spacing of 4.4 and 1.5 km, respectively. The driving global model and nested regional models were based on the Even Newer Dynamics for General atmospheric modeling (ENDGame) dynamical core (Wood et al. 2014). The driving model fields were taken from archived analysis from the operational MetUM global model [approximate horizontal grid spacing of 17 by 25 km in the tropics, with convection parameterized using the mass-flux scheme introduced by Gregory and Rowntree (1990) and with subsequent enhancements]. The 4.4 km nest was the same as that of the East Africa operational forecast model run by the Met Office in 2014 (Woodhams et al. 2018) and is shown in Fig. 1a. The 1.5 km nest (enclosed within the dashed line in Fig. 1a) was centered on Lake Victoria with approximate dimensions of 1500 km by 1500 km. The configuration of the regional models had 80 terrain-following vertical levels up to a lid of 38.5 km (lowest level ~1.5 m) and included the Aranami et al. (2015) mass restoration scheme, which reduces the excessive rainfall rates typical of MetUM models of this configuration (Lean et al. 2008; Kendon et al. 2012). Note that this scheme was not present in the MetUM configuration described in Woodhams et al. (2018), but was present in the configuration in Finney et al. (2019). Time steps of 100 and 60 s were used for the 4.4 and 1.5 km simulations, respectively.

Lake surface temperatures (LSTs) were prescribed as the foundation water surface temperature (temperature below the diurnal warm layer) taken from daily Operational Sea Surface Temperature and Sea Ice Analysis (OSTIA), available on a $1/20^\circ$ (~6 km) grid (Fiedler et al. 2014). For this dataset, LST observations are obtained from in situ data received via the Global Telecommunication System (GTS, although no in situ observations existed over Lake Victoria during this study) and satellite sea surface temperature (SST) data from the Group for High Resolution SST (GHRSST). A full discussion of this method and its limitations is given in Woodhams et al. (2018).

b. Observations

The simulated precipitation and OLR were compared to observations to ensure that the models were producing storms similar to observed. Observations from the IMERG Final Precipitation version 5 (V05) level 3 product from the Global Precipitation Measurement (GPM) mission (Huffman 2017; Huffman et al. 2018) were used. This product is available at 30 min intervals on a regular grid of 0.1° . The product combines and

TABLE 1. Simulation details of the cases studies.

Case	Start date	Run length	Period of interest	Description
Dry period	0000 UTC 9 Jul 2015	72 h	1200 LT 10 Jul–1200 LT 11 Jul 2015	Three-day period with no significant rain over Lake Victoria
Long rains storm	1800 UTC 5 May 2015	72 h	1200 LT 6 May–1200 LT 7 May 2015	Storm forms over land on the evening of 6 May and propagates onto Lake Victoria overnight
Dry season storm	1800 UTC 27 Jul 2016	72 h	1800 LT 28 Jul–1200 LT 29 Jul 2016	Storm forms over Lake Victoria during the early morning of 29 Jul

intercalibrates passive microwave (PMW) precipitation estimates from satellites in the GPM constellation with observations from the Dual-frequency Precipitation Radar (DPR) and a conical-scanning multichannel microwave imager [GPM Microwave Imager (GMI)] on board the GPM *Core Observatory*, using the method developed for the Tropical Rainfall Measuring Mission (TRMM) by Huffman et al. (2007) (Hou et al. 2014). Further algorithms are applied to the satellite data to improve rainfall estimates and spatial coverage. These are detailed in Huffman et al. (2018) and summarized here: calibration against the Global Precipitation Climatology Centre (GPCC) gauge analysis by Schneider et al. (2008); application of the National Oceanic and Atmospheric Administration (NOAA) Climate Prediction Center morphing technique with Kalman filter (CMORPH-KF) to estimate precipitation outside the sensed area by propagation of PMW estimates with motion vectors derived from geosynchronous IR satellite imagery (Joyce et al. 2004; Joyce and Xie 2011); and application of Precipitation Estimation from Remotely Sensed Information using Artificial Neural Networks–Cloud Classification System (PERSIANN–CCS), using IR retrievals calibrated against PMW retrievals (Sorooshian et al. 2000; Hong et al. 2004). Although GPM has been shown to outperform its TRMM predecessor, the product is known to have issues over high orography (Tang et al. 2016; Kim et al. 2017; Xu et al. 2017; Sungmin and Kirstetter 2018) and can underestimate high-intensity events (Wang et al. 2017; Sungmin et al. 2017).

Brightness temperatures T_b computed from the 10.8 μm IR channel from the Spinning Enhanced Visible and Infrared Imager (SEVIRI) instrument on board the Meteosat Second Generation satellite were also used (Schmetz et al. 2002; EUMETSAT 2012). These data are available at 15 min intervals with approximately 4 km grid spacing, but were interpolated onto a regular grid of 0.1° . For comparison with these observations, the model OLR was converted to a brightness temperature using the Stefan–Boltzmann relationship, $\text{OLR} = \sigma T_b^4$. It should be noted that the observed and modeled

brightness temperatures are not directly comparable since the observations only take into account wavelengths within the 10.8 μm IR channel.

Data from the European Centre for Medium-Range Weather Forecasts (ECMWF) interim reanalysis (ERA-Interim) (Dee et al. 2011) on a 0.7° grid with 37 pressure levels were also used to compute monthly mean profiles of winds and specific humidity. The profiles simulated by the MetUM show good agreement with the profiles from ERA-Interim reanalysis for the case study periods, allowing a direct comparison of the simulations to ERA-Interim.

3. Results

a. Case study introduction

Three case studies were analyzed for this study: one of a 3-day dry period taken from July 2015, one of a storm during the long rains season in May 2015, and one of a storm during the dry season in July 2016. Each case study was run out to 72 h, with output every 1 h. Details of the three case study simulations are summarized in Table 1. To choose the storm case studies, periods when storm events occurred in both GPM observations and the East Africa operational forecast model (UKMO 2017, unpublished data) were chosen, to increase the likelihood that the simulations would produce a storm of sufficient quality to analyze. Similarly, a 3-day dry period was identified in both the observations and model for the dry period case study.

1) DRY PERIOD (9–11 JULY 2015)

The dry period case is taken from the middle of the 2015 JJAS dry season, during a period in which almost no rain fell over Lake Victoria. This case is used to consider the baseline lake–land-breeze circulation, unperturbed by strong convective activity. On all three days of this simulation, both the synoptic-scale and lake–land-breeze circulation patterns over Lake Victoria were remarkably similar (not shown), therefore only results from midday on 10 July to midday on 11 July are analyzed. During the afternoon of 10 July, some

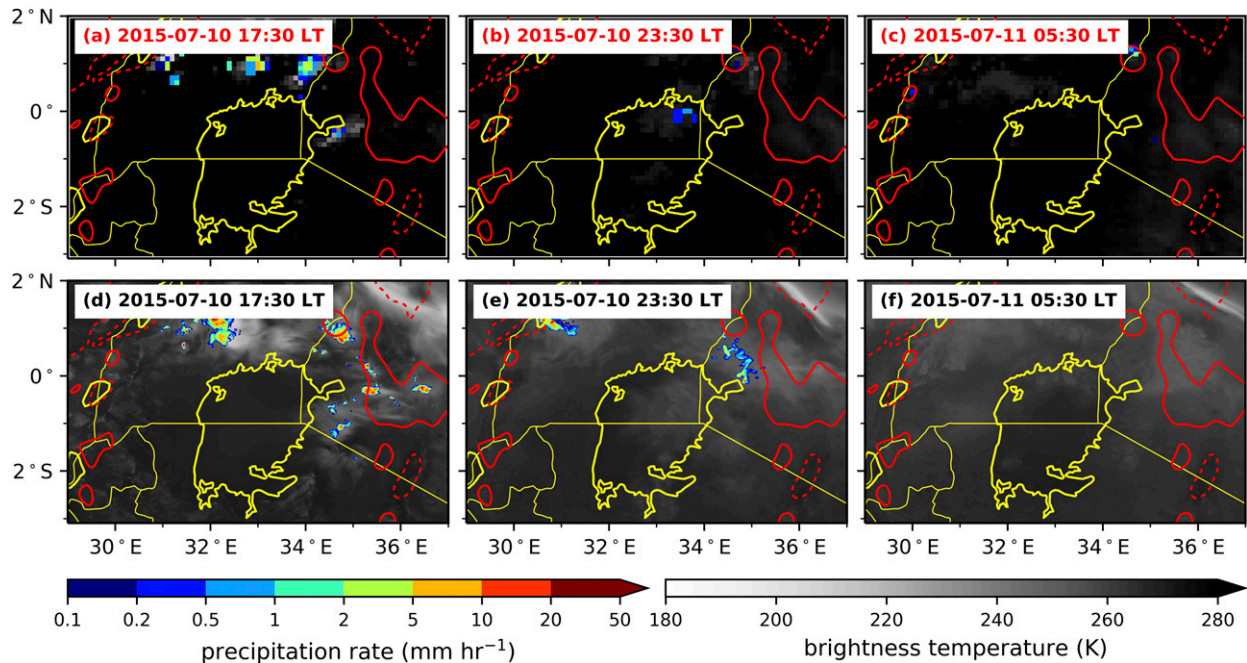


FIG. 2. (a)–(c) (red titles) Observed precipitation from GPM and observed $10.8\ \mu\text{m}$ brightness temperature from SEVIRI and (d)–(f) (black titles) simulated precipitation (colors) and brightness temperature computed from simulated OLR (grayscale) between 10–11 Jul 2015 (dry period). Red contours give orography at 1 (dashed) and 2 km (solid).

scattered convection occurred to the north and northeast of the lake (Figs. 2a,d), and overnight there was some cloud (reduced brightness temperatures) over the lake in both the model and observations (Figs. 2b,e). Given the relatively warm cloud-top temperatures, the cloud was likely low, although observations show a small area of light rain did occur over the north of the lake, which was not captured by the model. The lake was clear in both the model and observations during the early morning (Figs. 2c,f). Given that the model remained dry over the lake and produced precipitation over land comparable to the observations, it is considered that this simulation is suitable for investigating the lake–land-breeze circulation in relatively dry conditions.

2) LONG RAINS (LR) STORM (5–8 MAY 2015)

A similar pattern of storm activity occurred on all three days of this case study, taken from the 2015 long rains season. The storm that initiated on the evening of 6 May is investigated, since this storm was the most significant of the 3-day period. In both the observations and simulation, convection initiated along the eastern shore of Lake Victoria and to the northeast of the lake during the late afternoon (Figs. 3a,j). The convection along the eastern shore was observed to dissipate into the evening (Figs. 3b,c), while the convection to the northeast organized and deepened, with its southwestern edge extending over the northeast of the lake

(Figs. 3d,e). In the model, the convection along the eastern shore persisted into the evening (Figs. 3k,l). The convection to the northeast also organized in the model, but did not extend toward the lake (Figs. 3k–n).

The core of the observed storm moved westward from the land to the lake between 2330 and 0130 LT (Figs. 3d,e). The storm grew and rainfall rates increased, especially over the lake, during the early morning (Fig. 3f). As the storm continued to propagate westward through the morning, it formed large areas with rainfall exceeding $10\text{--}20\ \text{mm h}^{-1}$, with much of the heaviest rainfall over the lake (Figs. 3g,h). In the simulation, the convection along the eastern shore propagated westward over the lake from 2130 LT (Figs. 3l–o). This convection organized and deepened as it propagated, forming several embedded convective cells with rainfall rates exceeding $20\ \text{mm h}^{-1}$ along its leading edge. Similar to the observed storm, the greatest rainfall rates occurred over the northwest of the lake. However, the stratiform region of the simulated storm was situated over the lake to the south and east of the core, whereas it was observed over land to the north of the core.

Between 0730 and 0930 LT, the observed storm began to weaken, although widespread light rainfall persisted to the north of the storm (Figs. 3h,i). In the simulation, the storm began to dissipate once the leading edge reached the northwest shore, and some new convective initiation occurred to the north of the lake (Figs. 3q,r).

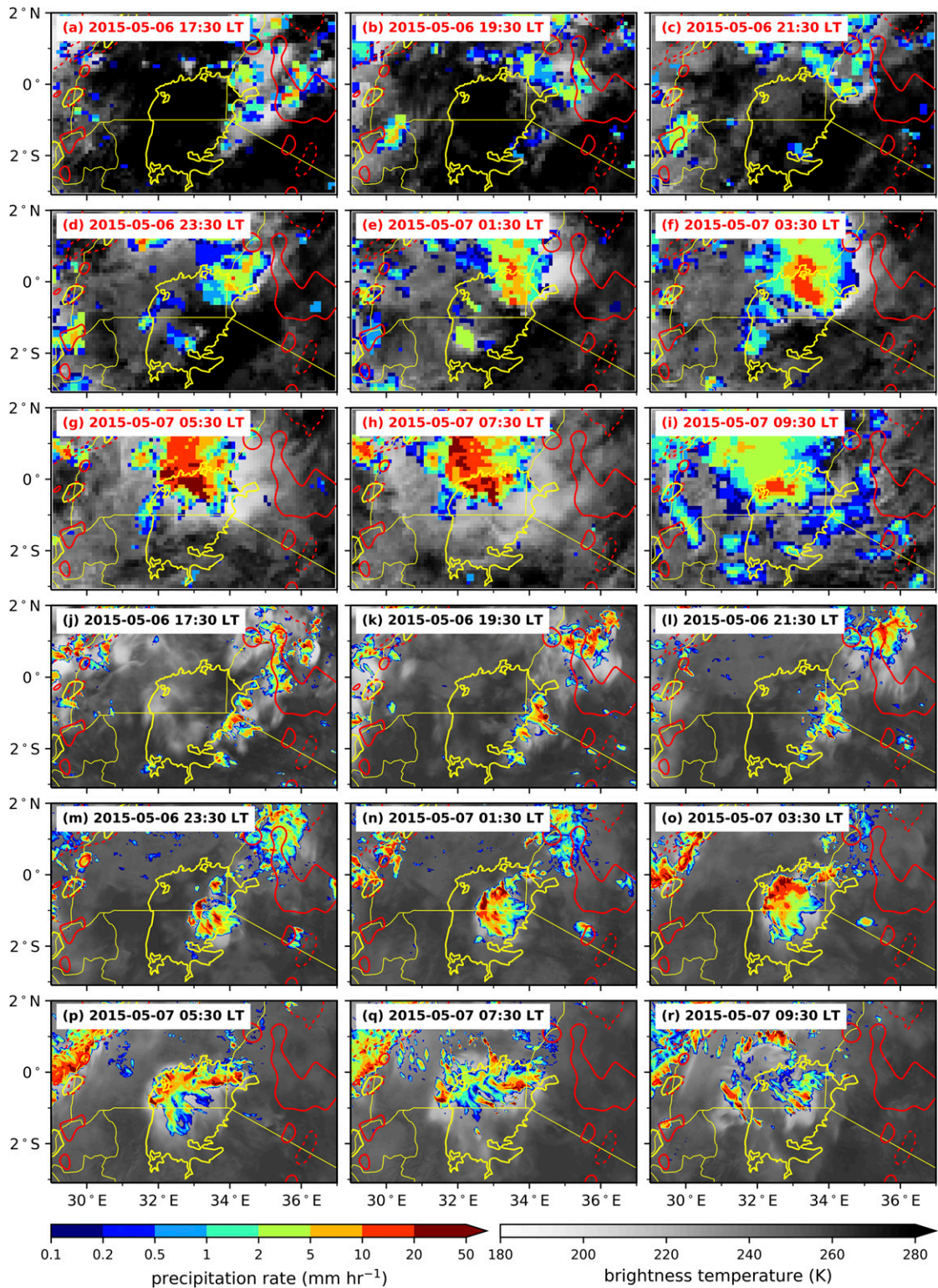


FIG. 3. As in Fig. 2, but for 6–7 May 2015 (LR storm) with (a)–(i) (red titles) showing observations and (j)–(r) (black titles) showing model data.

Although there are some large differences between the structure and location of the observed and simulated storms, the timing and propagation of the storms are similar. In particular, this simulation is appropriate to investigate the evening propagation of convection from land to lake.

3) DRY SEASON (DS) STORM (27–30 JULY 2016)

During this case, taken from the 2016 JJAS dry season, storms formed over the center of the lake during the early morning. Similar to the LR storm, a consistent pattern of precipitation occurred each day. The storm that initiated on the morning of 29 July is investigated in detail since it closely matched the observations (Fig. 4). Convection was initiated over the Kenyan Highlands (to the northeast of the lake) during the evening of 28 July and dissipated overnight in both the observations and simulation (Figs. 4a–d,j–o). Note that this storm persisted longer in the simulation than the observations. Convection also occurred to the northwest of the lake at this time, although over a much smaller area in the simulation compared to the observations. A significant storm also occurred in the northeast of the Democratic Republic of Congo (not shown). In both the observations and simulation, a storm initiated over the lake itself around 0630 LT (Figs. 4f,o). While the observed and simulated storms both initiated in the western sector of the lake, the simulated storm initiated approximately 100 km farther north. The storm grew and organized throughout the morning, propagating toward the southwest of the lake, with anvils sheared to the west (more so in the simulation) (Figs. 4g,h,p,q). The storm consisted of several rain cores, but these were smaller and more intense in the simulation, consistent with the bias found by Finney et al. (2019). The simulated storm had dissipated by 1530 LT, while there was still some rainfall associated with the dissipating storm in the observations at this time (Figs. 4i,r).

The good spatial and temporal agreement of the initiation and evolution of the storm over the lake between the simulation and observations make this simulation ideal for investigating an isolated storm over the lake.

While there is generally good agreement between the simulations and reality in all cases, it should be noted that excellent agreement is not essential. A greater importance is placed on sampling a good variety of conditions and types of storm, which these chosen case studies achieve.

b. Case study: Dry period

Figure 5a shows that the mean prevailing 10 m wind direction is southeasterly across the Lake Victoria basin

during the dry period case study. The near-surface air over land is generally dry, especially to the south of the lake, whereas air over the lake itself has high specific humidity.

The horizontal structure of the lake–land-breeze circulation near the surface is shown in the diurnal cycle of 10 m wind and 1.5 m specific humidity q (Fig. 6). The vertical structure of the circulation is shown in mean cross sections of the horizontal and vertical wind, virtual potential temperature θ_v (a proxy for density), and q (Fig. 7). The transects along which the mean cross sections are computed are perpendicular to the eastern shore of Lake Victoria and shown by the lines in Fig. 1b. The lake lies between approximately 0 and -220 km on the horizontal scale. In Figs. 7a–f, the along-transect wind (shading) is shown as an anomaly from the mean daily (24-h) flow at that location, to illustrate the local circulation only and make the lake–land-breeze circulation easier to identify. Arrows show the actual wind. Maps of CAPE and CIN during the morning and evening of the case study are shown in Fig. 8.

The boundary layer (BL) over the lake is characterized by high q throughout the day, due to strong evaporation from the lake surface (Figs. 6 and 7g–i). At midday, both the actual wind and the wind perturbation from the diurnal mean are southeasterly across the lake (Figs. 6a and 7a). At this time, air above the lake has lower θ_v relative to the nearby land, despite its greater moisture content, reflecting its lower temperature (Fig. 7g).

During the afternoon, the contrast in θ_v between the lake and land increases due to greater daytime heating of the air over land (Figs. 7h,i). Around 1500 LT, a lake breeze A forms over the lowest 1 km above the lake (Figs. 6b and 7b) and advects moisture from the lake BL onshore (Figs. 6b and 7h). The divergence over the lake results in broadscale subsidence above the lake surface (Fig. 7n). The moisture content of the air over land increases and dry convective eddies B deepen the BL to ~ 4 km MSL to the east of the lake (Figs. 7h,n).

The onshore flow across the eastern shore of the lake is opposed by the prevailing southeasterly winds over the lowest ~ 6 km of the atmosphere and the lake-breeze front penetrates only 20–30 km onshore at 1500 LT (Figs. 7b,h). However, the wind anomaly is upslope across the extent of the highlands, suggesting that an anabatic component of wind is working against the prevailing flow (Fig. 7b). Shallow cumulus form where the lake-breeze front penetrates almost 200 km onshore in the west (Figs. 7b,h,n). To the east of the lake, shallow cumulus form farther inland than the lake-breeze front, instead associated with the dry convective eddies (Fig. 7n).

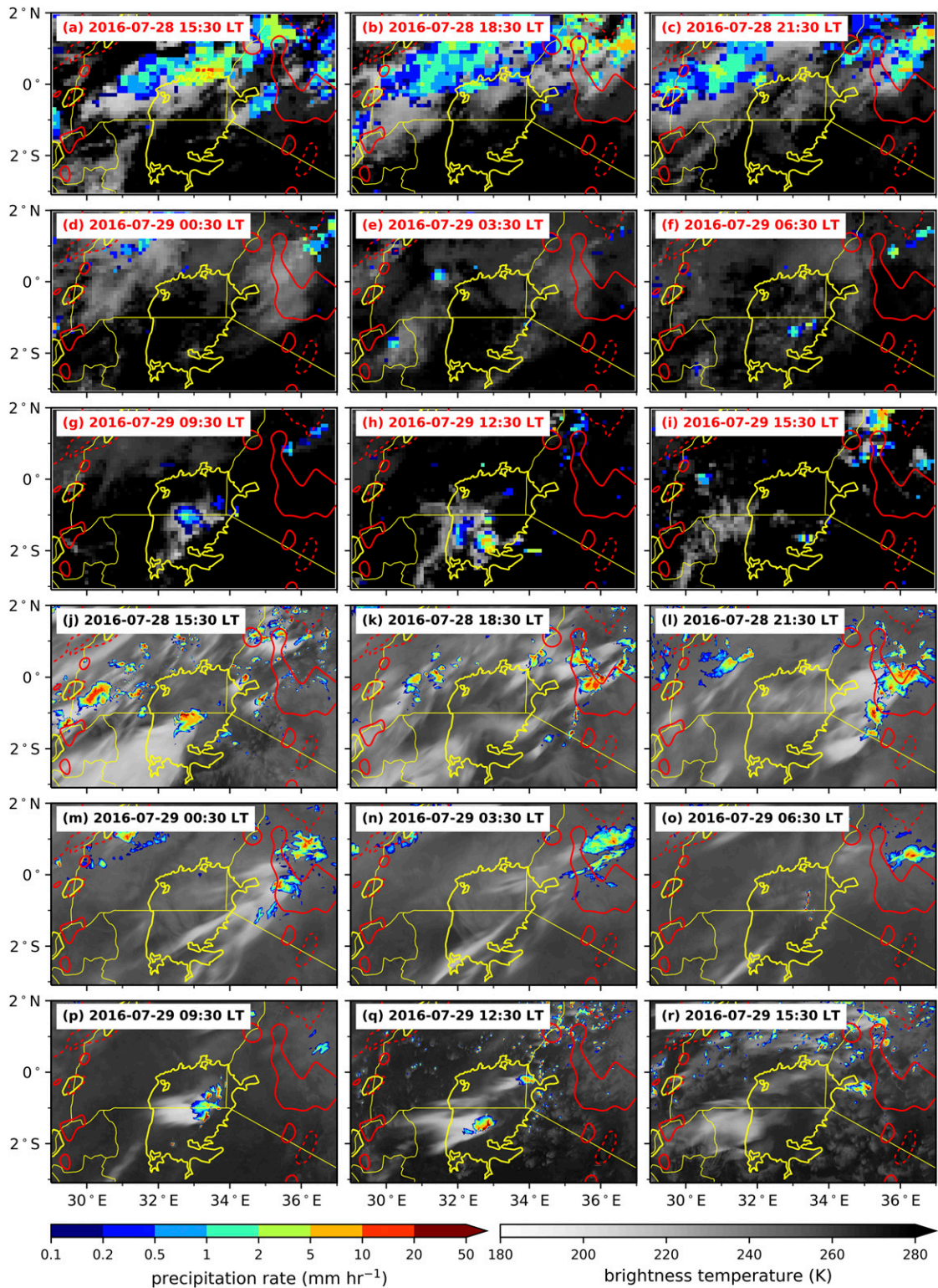


FIG. 4. As in Fig. 2, but for 28–29 Jul 2016 (DS storm) with (a)–(i) (red titles) showing observations and (j)–(r) (black titles) showing model data.

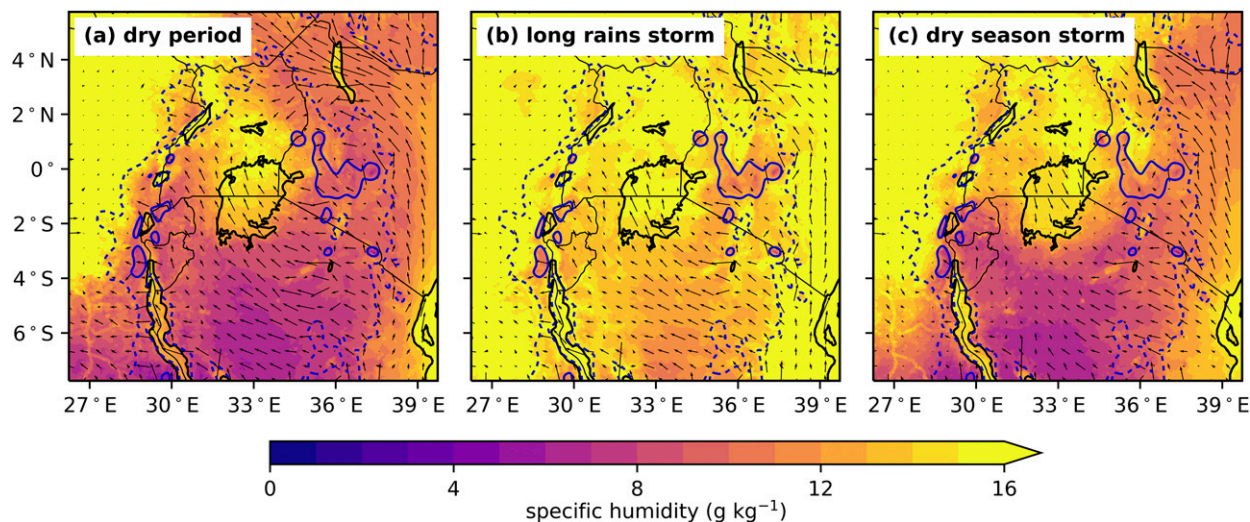


FIG. 5. Mean simulated 10 m winds (vectors) and 1.5 m specific humidity (shading) over a 24 h period from 1200 LT (a) 10 Jul 2015, (b) 6 May 2015, and (c) 28 Jul 2016 for the dry period, LR storm, and DS storm respectively. Blue contours give orography at 1 (dashed) and 2 km (solid).

Around 1800 LT, θ_v reaches a maximum over land, and is particularly high approximately 80 km to the east of the lake (Fig. 7i). This marks the leading edge of the lake breeze (Fig. 7c), beyond which the air is well mixed up to 3.5 km MSL (Fig. 7i). As the turbulent eddies subside (Fig. 7o), the prevailing winds from the east, where air is cooler and drier, accelerate and oppose the lake breeze (Figs. 7c,i). Strong ascent occurs where the lake breeze and prevailing winds converge (Fig. 7o). While there is some CAPE to the east of the lake, CIN is also high, so deep convection is suppressed (Figs. 8a,d).

By 1800 LT, a strong return flow of the lake breezes over both shorelines is established between 3–5 km MSL; on the lake side of the eastern convergence line, a branch forms back toward the lake (C) and, on the land side, a branch flows toward the mountains (D) (Fig. 7c). The lake-side return flow advects moisture from the land BL back toward the lake (Fig. 7i).

Following sunset, the surface air cools, in particular over the land, and the gradient in θ_v reverses between the lake and land (Fig. 7j). To the east of the lake, the southeasterly wind accelerates and low θ_v air from east of the Kenyan Highlands is advected toward the lake over a depth of ~ 2 km (Figs. 7d,j). Over the lowest few hundred meters, a land breeze E also forms at the eastern shoreline (Figs. 7e,k). By 0200 LT, the land breeze is encompassed by the prevailing southeasterly flow, which likely includes a katabatic component. The front and upper boundary of this density current are not well defined, therefore E roughly marks the land-breeze front in Figs. 7k and 7l.

Driven by the offshore flow, the convergence line to the east of the lake begins to propagate westward, crossing the lake shore at approximately 2200 LT (Figs. 6d and 7d). The return-flow pattern (C, D) between 3 and 5 km MSL is tied to the convergence and therefore also propagates toward the lake (Fig. 7d). Uplift occurs at and ahead of the convergence (Fig. 7p), where moist air over the lake is pushed up from the surface into a shallow bulge F (only a few hundred meters in depth) as the density current from the land runs into the stable layer over the lake (Fig. 7j). Although there is no actual offshore flow over the western shoreline at 2200 LT, the retreating westerly lake breeze (pushed back across the lake by the offshore flow from the east) means that the wind perturbation relative to the diurnal mean is offshore (Figs. 6d and 7d).

The convergence, and leading edge of the moisture bulge, propagate westward across the lake, reaching the lake center at ~ 0200 LT (Figs. 7e,k,q). A very shallow land breeze G (limited to only the lowest ~ 300 m) forms across the western shore (Figs. 6e and 7e,k). The return flows above the convergence (C, D) are now both toward land, such that there is midlevel divergence over the center of the lake (Fig. 7e). Despite vertical motion and upward transport of moisture, there is no CAPE over the lake (except for some small patches to the north) so deep convection is suppressed (Fig. 8g).

The leading upper edge of the moisture bulge F coincides with the upper boundary of the low- θ_v air advected from the east. The center of the bulge appears to propagate westward with a more well-defined density current (likely the land breeze E) at low levels, and is

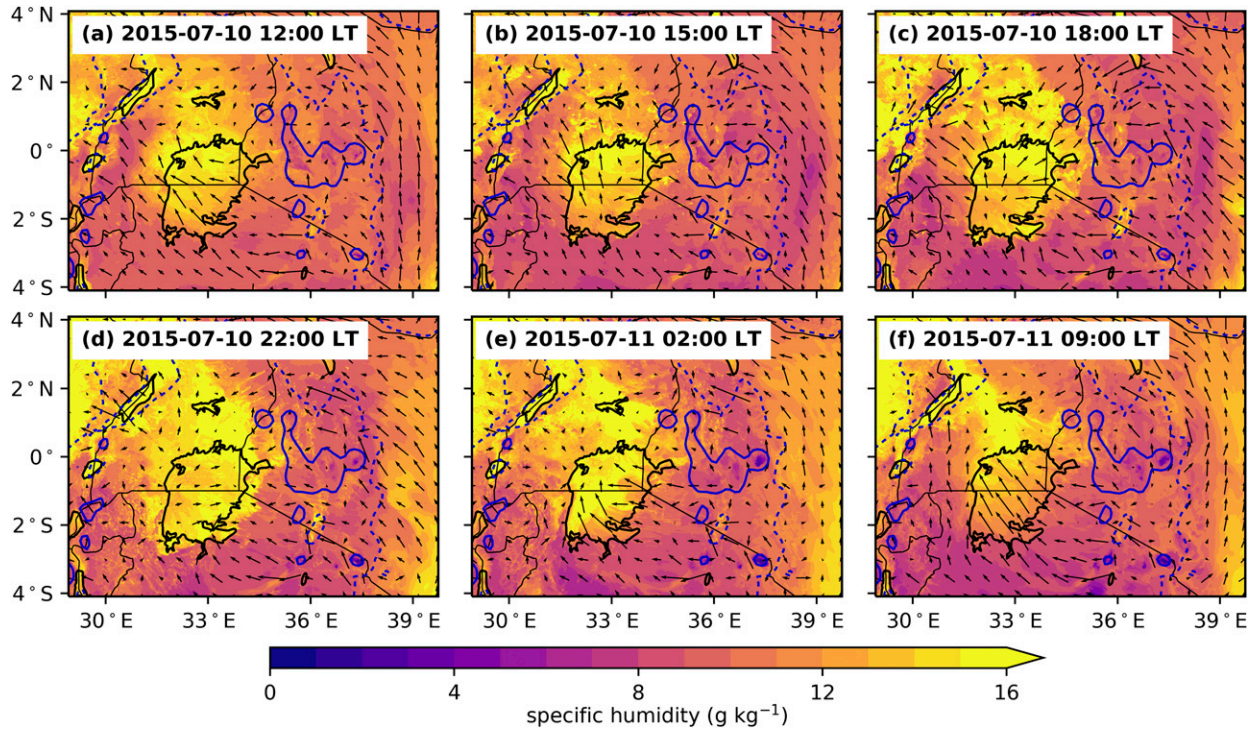


FIG. 6. Simulated 10 m winds (vectors) and 1.5 m specific humidity (shading) during the dry period case study. Blue contours give orography at 1 (dashed) and 2 km (solid).

bounded to the west by the westerly land breeze G (Fig. 7k). As such, the bulge grows horizontally. It also grows in height, in particular at the leading edge, exceeding 1 km at 0200 LT.

During the night, the specific humidity of air between ~2–5 km above sea level over the lake is also elevated relative to the surroundings (Figs. 7j–l, H). Although there is vertical motion up to this height over the lake, this increased moisture appears unrelated to the low-level moisture bulge. Rather, it exists due to westward advection of moist air from the daytime BL over land by the westward return flow of the lake breeze C on the preceding evening. Due to shear in the eastward return flow of the land breeze D (Figs. 7d–f), the top layer of moist air over the lake is advected back toward land (between 0 and +200 km, Figs. 7j–l).

Through the early morning, the easterly winds strengthen again to the west of the lake and prevail across the whole lake by 0900 LT (Figs. 6f and 7f). However, the wind perturbation across the western shore remains eastward, so there is shear across the lowest 1 km above this region and the top of the bulge F propagates ahead of the lower leading edge (Figs. 7f,l). As the bulge propagates onshore, the depth of the moist air increases, but the bulge loses its individual identity as

it merges with the daytime deepening of the land BL (Figs. 7f,l,r).

c. Case study: Long rains storm

During this case study, a storm forms inland of the eastern shore of Lake Victoria during the evening and propagates across the lake overnight. The near-surface large-scale wind field preceding the storm is very similar to that of the dry period, with prevailing southeasterlies across the lake (cf. Figs. 5a,b). However, the near-surface air has much higher specific humidity relative to the dry period case, especially over land.

The prevailing wind over the lake during the day is disrupted by a storm A over the northwest of the lake, which has persisted from the previous night. (Figs. 9a,b,m,n). However, a lake breeze B still forms over both the eastern and western shorelines around 1500 LT (Figs. 9b,h). As in the dry period case, the lake breeze across the eastern shore converges with the southeasterly prevailing winds and the lake-breeze front is prevented from penetrating far inland (Fig. 9b). Deep moist convection C initiates along the convergence line and precipitation occurs over the foothills of the Kenyan Highlands (Fig. 9n). Pockets of high CAPE (exceeding 1000 J kg^{-1}) exist over this region, as well as areas of CIN

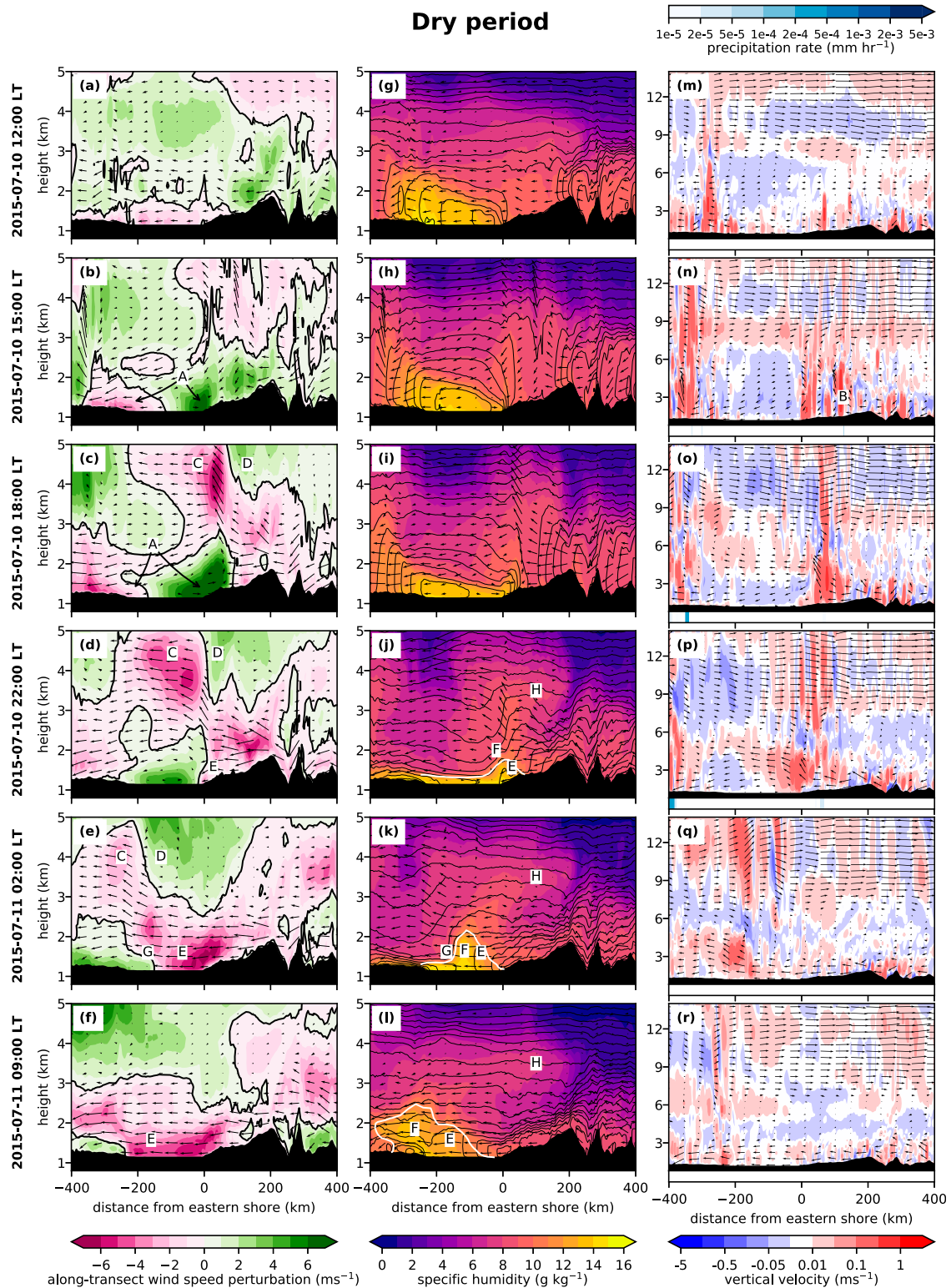


FIG. 7. Cross sections of (a)–(f) simulated along-transsect wind speed anomaly, computed with respect to the 24 h mean at each grid point (shading, positive for northwesterly anomalies), (g)–(l) specific humidity (shading) and virtual potential temperature (contours), and (m)–(r) vertical wind speed (upper panel) and precipitation rate (lower panel) along a transect perpendicular to the eastern shore of Lake Victoria (averaged over the black lines in Fig. 1b) during the dry period case study. Actual wind vectors (not anomalies) in the along-transsect and vertical directions are shown by the arrows. The white contour in (g)–(l) roughly marks the boundary of the moisture bulge described in section 3b. Black contours in (m)–(r) show regions where the sum of the cloud liquid water content and cloud ice content exceeds 0.1 g kg^{-1} . Labels A–H are described in the text.

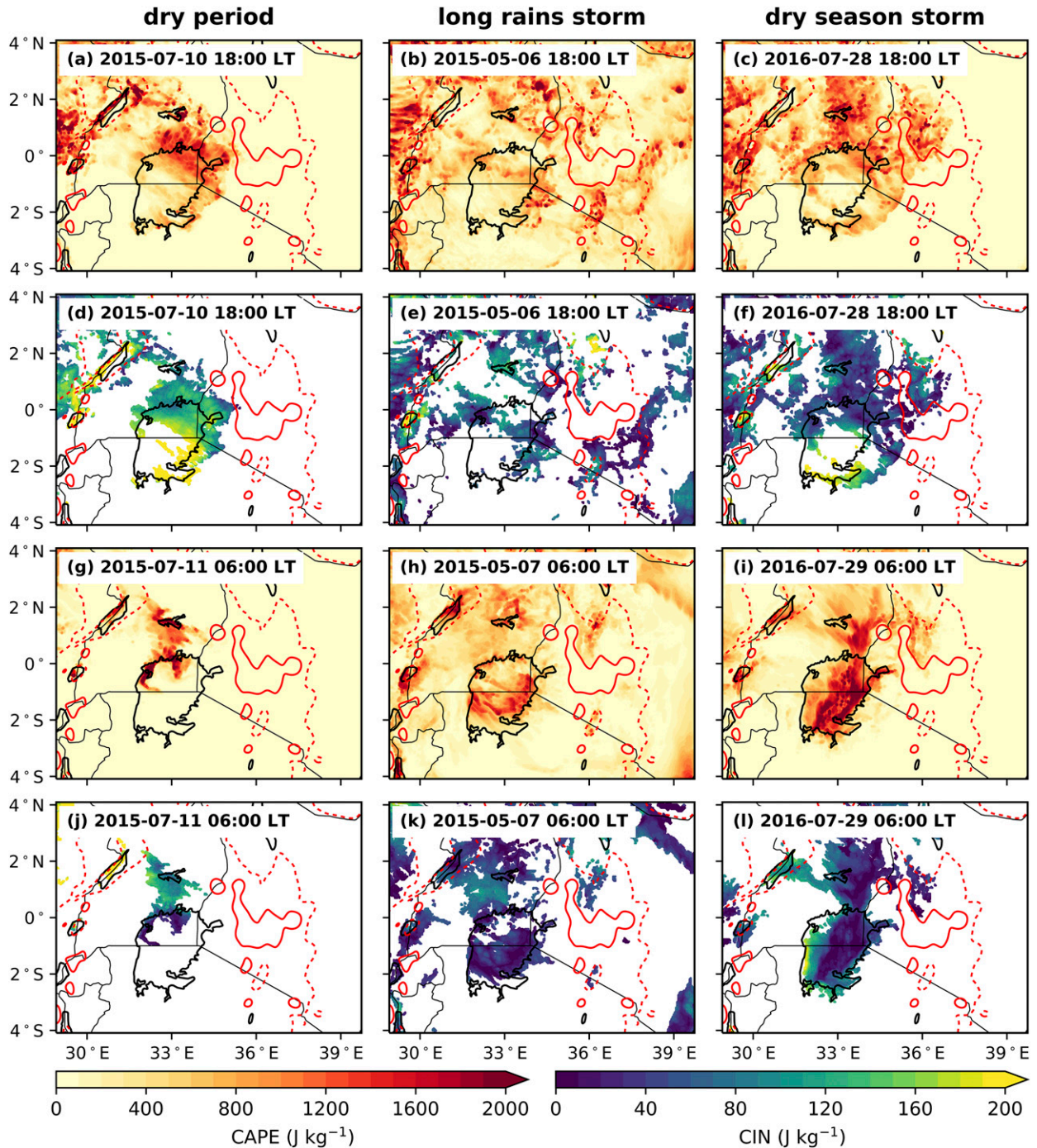


FIG. 8. Maps of (a)–(c),(g)–(i) CAPE and (d)–(f),(j)–(l) CIN (only plotted where CAPE > 400 J kg⁻¹) for (a)–(f) 1800 LT and (g)–(l) 0600 LT for the (left) dry period, (middle) LR storm, and (right) DS storm. CAPE is computed using a parcel from 70 m above the surface. Red contours give orography at 1 (dashed) and 2 km (solid).

exceeding 100 J kg⁻¹ (Figs. 8b,e), showing that there is sufficient dynamical triggering to overcome the CIN and initiate deep convection. The convection is invigorated by the very moist air shown by the low contrast in specific humidity over the land and lake

relative to the dry case (cf. Figs. 9g–l and 7g–l). The region of convergence beneath storm C remains almost stationary into the evening, as the convection deepens, organizes and a larger, contiguous area of precipitation forms (Figs. 3l,m and 9c,d,o,p).

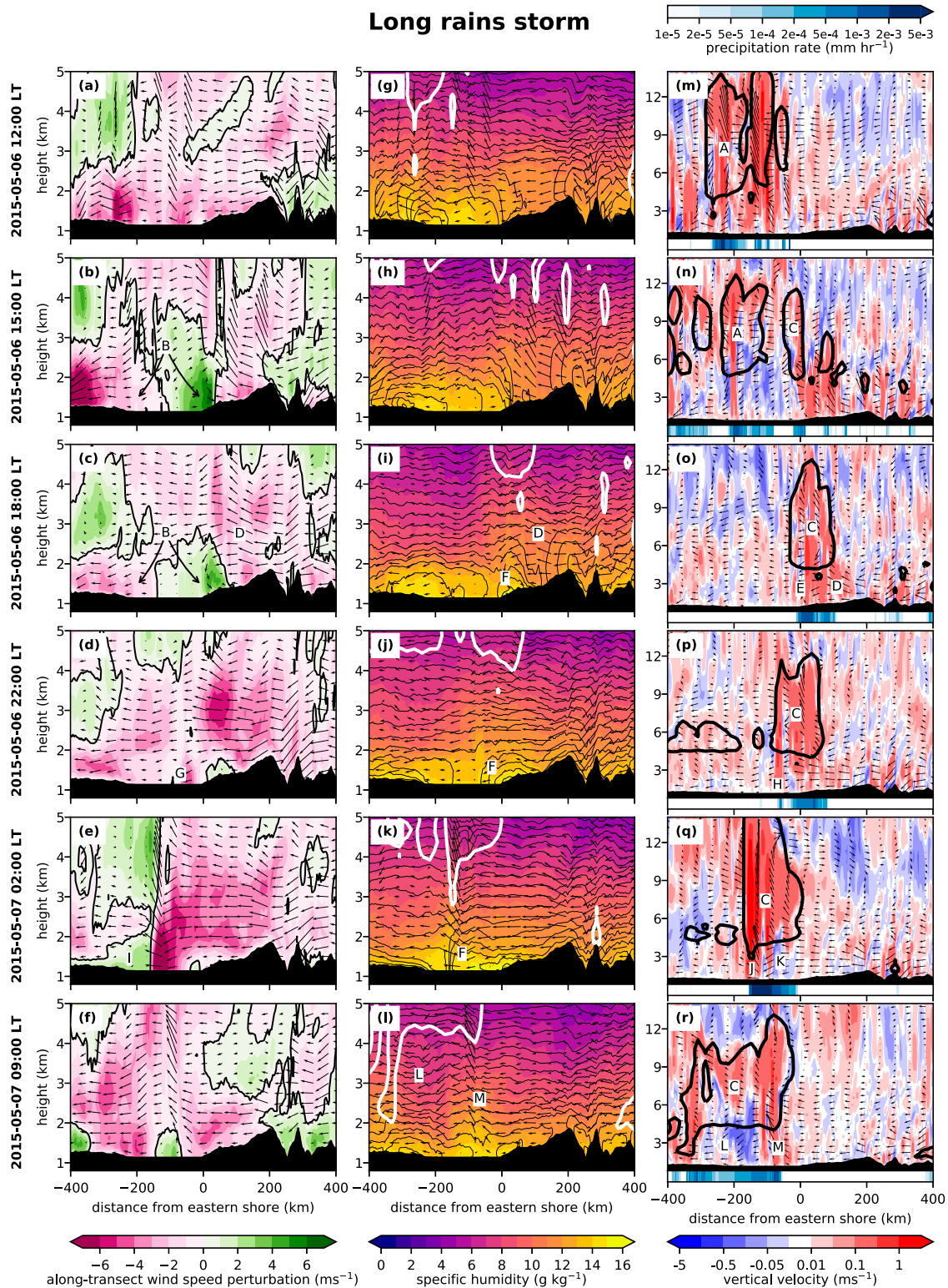


FIG. 9. As in Fig. 7, but during the LR storm case study. Note, white contours in (g)–(l) now show the same as the black contours in (m)–(r). Labels A–M are described in the text.

The deep convection disrupts the return flow of the lake breeze (between 2 and 4 km above the lake surface) such that it is less defined relative to the dry case (cf. Figs. 9c and 7c). The moist air from over land is transported vertically by the moist convection, rather than being advected back over the lake (Figs. 9h–j,n–p). During the initial stages of the storm, much of the inflow originates from the mountains to the east and flows into the rear of the storm, over a depth of approximately 4 km (Figs. 9b–d,h–j,n–p, D).

Around 1800 LT, a downdraft E begins to form beneath the storm, located just over the eastern shoreline (Fig. 9o). Beneath the downdraft, a density current F forms and propagates toward the lake (Fig. 9j). Given that θ_v and q directly below the storm do not change, it is likely that the density current corresponds to the formation of a land breeze, rather than cold pool outflow from the storm. Similar to the dry period, this density current forms ahead of the cooler air to the east, but the two flows merge by 2200 LT, when the southeasterly winds accelerate (Figs. 9c,d,i,j).

Southeasterly winds prevail throughout the atmospheric column (i.e., there is low shear) at 2200 LT, such that the leading edge of the storm propagates along with the density current (Figs. 9d,j,p). Convergence occurs at the leading edge of the density current (G, ~ 70 km west of the eastern shore) due to deceleration as the eastern land-breeze front runs into the rear end of the lake breeze across the western shore (Fig. 9d). A new updraft H forms here and lofts moist air from above the lake surface into the storm as the rear inflow (consisting of air from over the land) is reduced (Figs. 9j,p).

The storm C continues to grow in height and horizontal extent throughout the evening (Fig. 9q). At 0200 LT, a land breeze I forms across the western shore and converges with the easterlies at the leading edge of the storm (composed of the prevailing winds and eastern land breeze and strengthened by the downdraft outflow) (Figs. 9e,k,q). The convergence strengthens the updraft at the storm's leading edge, increasing the transport of moist lake BL air into the storm (Fig. 9k). High CAPE and low CIN over the lake (Figs. 8h,k) encourage storm growth, such that the top of the storm extends to a height of over 15 km MSL (Fig. 9q). Rainfall rates are greatest at the leading edge of the storm, which is situated ~ 150 km from the eastern shore, and along which an arcus cloud J forms (Fig. 9q). To the rear of the storm, inflow is reduced further as a large region of downdraft K forms ~ 100 km behind the leading edge (Fig. 9q).

As the storm continues to propagate westward, the land breeze from the west retreats (Fig. 9f). By 0900 LT, the storm loses organization and its cloud-top height is

greatly reduced, as are the size and strength of its updrafts (Figs. 3r and 9r). Behind the large arcus cloud centered at -350 km on the horizontal scale, there is a large downdraft L extending across almost 200 km, (Fig. 9r). The downdraft forms a cold pool, shown by the low θ_v air and reduced specific humidity below the storm (Fig. 9l). Although the storm is dissipating, a new updraft M forms at the rear, over the moist supply of air above the center of the lake (Figs. 9l,r). However, the updraft weakens during the late morning as divergence occurs over the lake due to the formation of lake breezes across both shores (not shown).

d. Case study: Dry season storm

During this case study, the mean 10 m wind field over the lake differs to the previous two cases, with northwesterly winds (as opposed to southeasterly) prevailing over the northwest of the basin and the lake itself (cf. Fig. 5c to Figs. 5a,b). However, to the south and east of the lake, the large-scale circulation pattern is similar to the previous cases. The near-surface moisture during the DS storm case is similar to the dry period case (although there is increased specific humidity to the north of the lake in the former case). This similarity is to be expected since both cases are taken from the same time of year.

In this case study, a storm initiates over the center of the lake during the early morning. During the preceding evening, lake breezes A occur over the northwestern and eastern shores, advecting moisture onto the land (Figs. 10a,g). Convection occurs along the lake-breeze fronts, where there is high CAPE and low CIN (Figs. 4k and 8c,f). Note that the large storm to the east (over the highlands, Fig. 4k) is not captured within the transect in Fig. 10. However, some small convective cells B do occur within the transect (Figs. 4k and 10m). The moisture for these is provided by the lake breeze, since the air to the east of the lake (at $> +150$ km) is very dry (Fig. 10g).

During the preceding evening, a large storm also occurs in the northeast of the Democratic Republic of Congo (not captured in the transect), a region which is generally very moist as it is under the influence of the Congo air mass (not shown). The storm deposits particularly cool (and therefore low θ_v) air C in this region (Fig. 10h). As such, a strong land breeze D forms over a depth of ~ 1 km across the western shore at 2200 LT (Figs. 10b,h). The land breeze advects the moist air from the Congo region toward the lake.

The northwesterly land breeze is opposed by weaker offshore flow across the eastern shore E, consisting of the easterly land breeze embedded within the prevailing southeasterlies (Fig. 10b). At 2200 LT, a moist bulge F begins to form at the convergence between the two land breezes, close to the eastern shore (Figs. 10b,h). As the

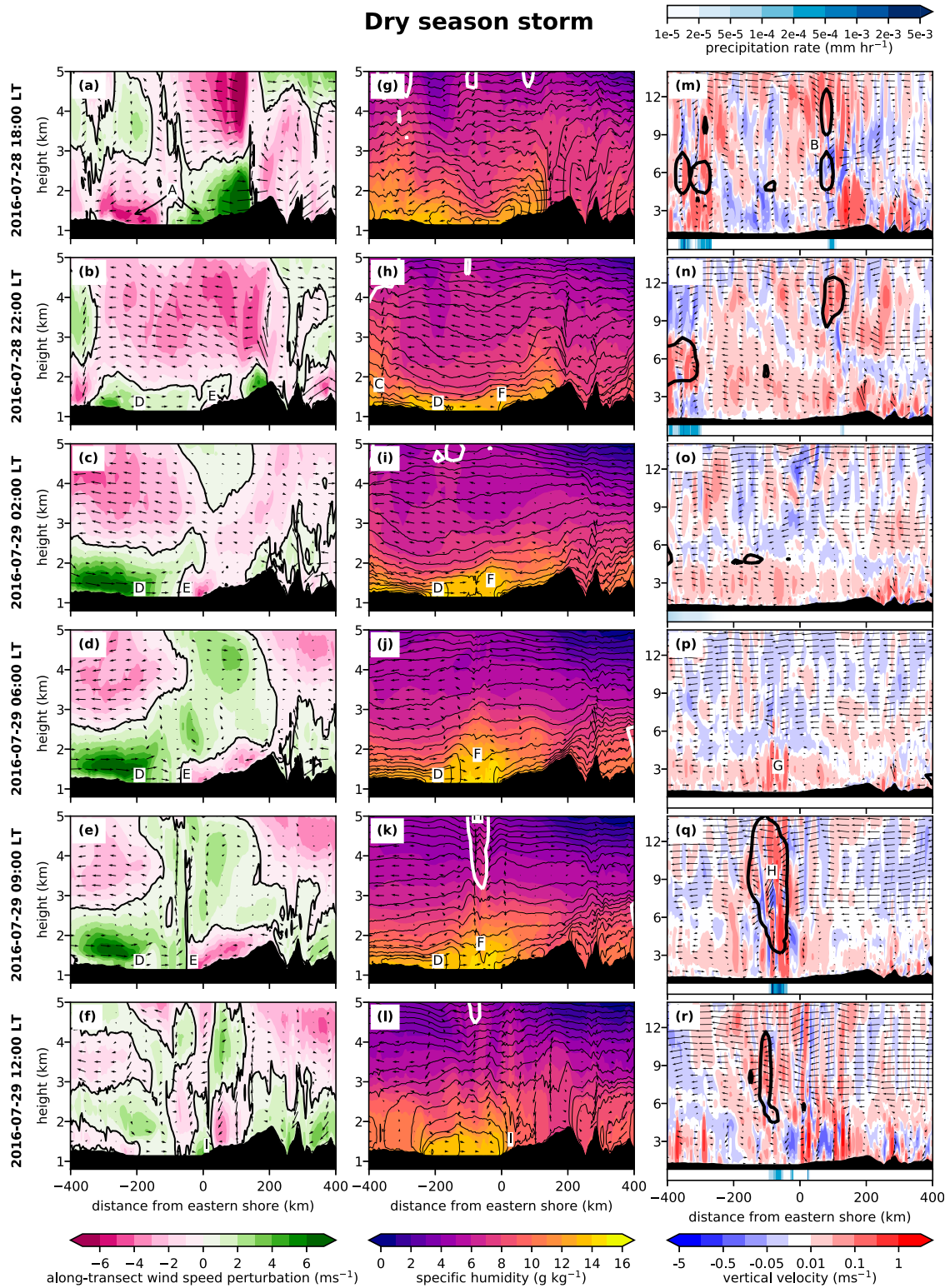


FIG. 10. As in Fig. 9, but during the DS storm case study. Labels A–I are described in the text.

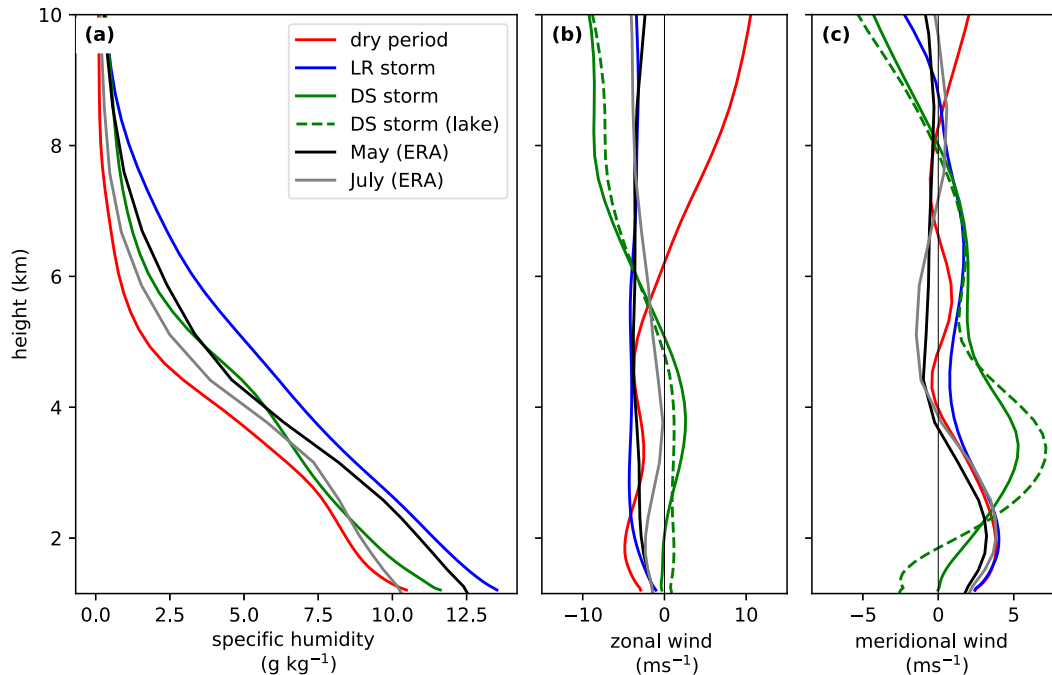


FIG. 11. (a) Mean specific humidity, (b) mean zonal wind, and (c) mean meridional wind taken over a 24 h period from 1200 LT 10 Jul 2015, 6 May 2015, and 28 Jul 2016 for the dry period, LR storm, and DS storm respectively. Climatological monthly means for May and July from ERA-Interim (1997–2016) are also shown (Dee et al. 2011). The solid lines correspond to the mean over the region within the solid box in Fig. 1a and the dashed line corresponds to the mean over Lake Victoria.

easterly flow strengthens between 2200 and 0200 LT, the convergence moves to approximately 50 km west of the eastern shore, as does the center of the moist bulge (Figs. 10c,i). This region of convergence remains stationary, and the bulge deepens, between 0200 and 0900 LT. (Figs. 10c–e,i–k). The strength of the western land breeze prevents westward propagation of the convergence, despite the southeasterly prevailing winds.

At 0600 LT, there is strong vertical motion *G* associated with the moist bulge *F* (Figs. 10j,p). High CAPE and low CIN over the lake (Figs. 8i,l) allow deep convection *H* to be triggered above the bulge between 0600 and 0900 LT (Figs. 10k,q).

The land breeze from the west weakens during the late morning, as the temperature gradient between the lake and the land reverses (Figs. 10f,l). The convergence line at the surface is pushed back toward the eastern shoreline by the development of a lake breeze *I* (Figs. 10f,l). However, the storm does not follow the low-level convergence due to the wind shear caused by the persisting southeasterlies at upper levels (Figs. 10f,l,r). As a result, the storm loses its moist air supply and the storm dissipates.

e. Case study comparison

Some differences between the case studies may be explained by the differing mean specific humidity

profiles of the atmosphere during each period (Fig. 11a). Climatologically, *q* is increased throughout the atmospheric column during May relative to July (black and gray lines respectively in Fig. 11a). The difference is greatest at the surface, where *q* is increased by $>2 \text{ g kg}^{-1}$ in May. This difference is symptomatic of the former lying in the MAM long rains season and the latter during the JJAS dry season. The moisture profile for the May case study compared to the July case studies reflects these climatological differences (cf. blue line to red and green lines). However, *q* at the surface is $\sim 1 \text{ g kg}^{-1}$ greater than the May mean during the LR case (cf. blue and black lines) and $\sim 1.5 \text{ g kg}^{-1}$ greater than the July mean during the DS storm case (cf. green and gray lines), demonstrating the importance of additional moisture for storm initiation.

In general, the climatological zonal and meridional winds show little change between May and July, although the midlevel zonal component is almost zero during July (Figs. 11b,c, compare black and gray lines). Below 4 km, the wind direction is predominantly southeasterly across the region (Figs. 11b,c). The case study profiles are similar to the climatologies at mid-levels and below, apart from the DS storm. During this case, zonal winds below 5 km are predominantly from the west and, over the lake, winds in the lowest $\sim 700 \text{ m}$

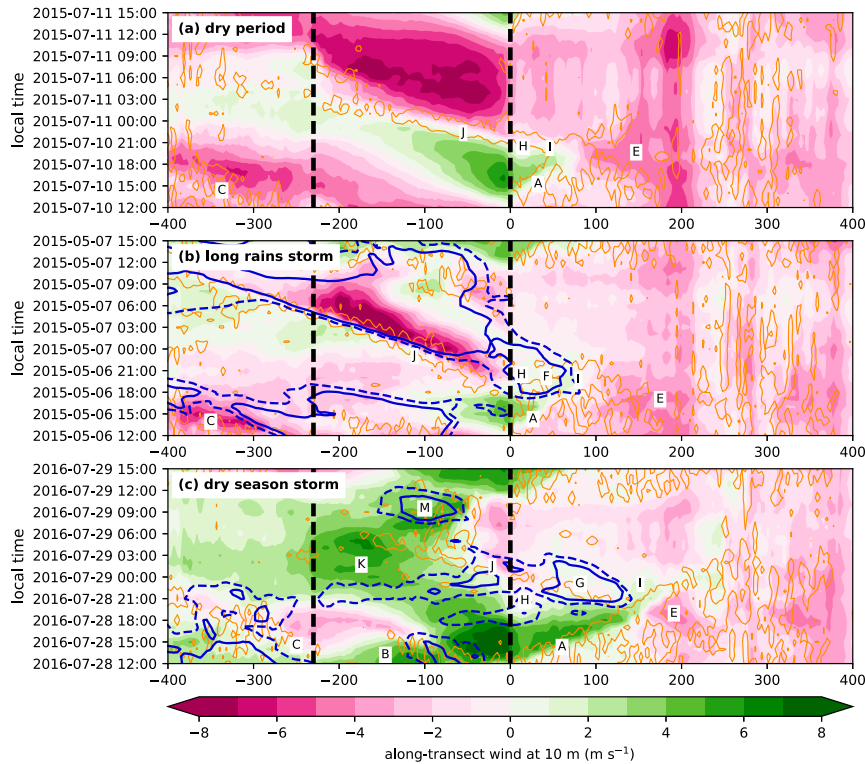


FIG. 12. Hovmöller of simulated along-transect 10 m wind speed for (a) the dry period, (b) the LR storm, and (c) the DS storm. Orange contours show regions with vertical velocity greater than 0.05 m s^{-1} at 1000 m AGL and blue contours show regions of OLR less than 200 (dashed) and 170 (solid) W m^{-2} . The black dashed lines show the boundaries of Lake Victoria. Labels A–M are described in the text.

have a component from the north. At upper levels, the wind profiles during the case studies vary significantly from one another and from the monthly climatologies, suggesting high day-to-day variability. There is almost no shear across the atmosphere during the LR storm, but high shear during the DS storm (cf. blue and green lines). The lack of shear in the former was shown to propagate the storm with the low-level convergence, increasing its longevity. In the latter case, the shear decoupled the convergence and storm, causing the storm to dissipate.

Differences between the cases are also highlighted in Hovmöller plots along the transect defined in Fig. 1b (Figs. 12 and 13). The along-transect 10 m wind shows many similarities between the dry period and LR case studies (Figs. 12a,b). Lake breezes A initiate across the eastern shore around 1200 LT and propagate ~ 80 km onto the land (green shading to the right of the 0 km dashed line), advancing at $\sim 3 \text{ m s}^{-1}$ (although the speed is more variable in time during the dry period). Preceding the DS storm, the eastern lake breeze A forms at a similar time, but propagates 160 km farther inland and at a greater, but more variable, speed

($\sim 4.5\text{--}6.5 \text{ m s}^{-1}$), as it is reinforced by anomalously strong wind B across the lake from the northwest (Figs. 12c and 13c).

Lake breezes C also form across the western shore, just before 1200 LT, and propagate ~ 240 km to the west in the dry period and LR storm case studies (Figs. 12a,b). The anomalously low θ_v air to the northwest D preceding the DS storm delays, weakens, and reduces the extent of the western lake breeze C (Figs. 12c and 13c).

The lake breezes (A, C) advect moist (thick black contours), low θ_v (green/blue shading) air away from the lake surface and onto the land (Fig. 13). In the dry period and DS storm case studies, the air over land is much drier than over the lake, creating a sharp gradient in moisture along the lake-breeze fronts (Figs. 13a,c). Air over land is already moist in the LR case study, so the gradient is weaker (Fig. 13b). There are no strong gradients in θ_v , since the cooler lake air warms as it propagates over land, eroding the front of the density current (Fig. 13).

In all three cases, the lake breeze across the eastern shore converges with the prevailing southeasterly winds, which are particularly strong on the slopes of

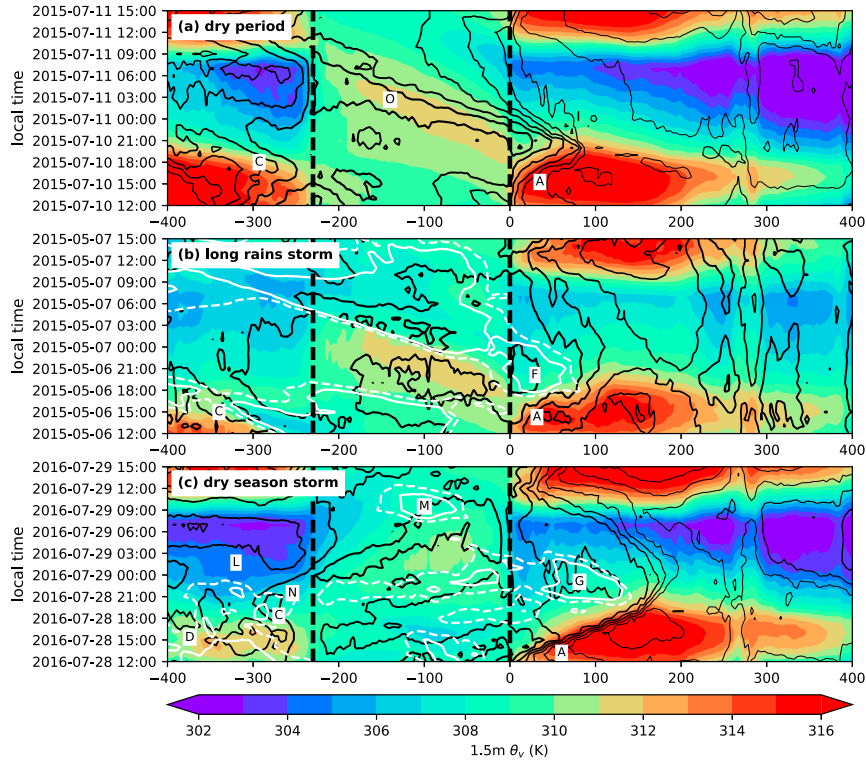


FIG. 13. Hovmöller of simulated 1.5 m virtual potential temperature θ_v , averaged over the transects in Fig. 1b for (a) the dry period, (b) the LR storm, and (c) the DS storm. Black contours give 1.5 m specific humidity with intervals of 1 g kg^{-1} (thicker lines show higher specific humidity) and white contours show regions of OLR less than 200 (dashed) and 170 (solid) W m^{-2} . The black dashed lines show the boundaries of Lake Victoria. Labels A–N are described in the text and match those in Fig. 12.

the Kenyan Highlands E (Fig. 12). Upward motion occurs along the convergence (orange contour between 0 and $\sim +100$ km, Fig. 12). In the two storm cases, the upward motion results in deep convection (low OLR, shown by blue/white contours between 0 and $+100$ km, Figs. 12b,c and 13b,c). The LR storm is labeled F and the land storm during the DS storm case study is labeled G. Whereas the air is already fairly moist over land during the LR storm, the moisture source for the storm over land in the dry season is air advected from the lake by the lake breeze (Figs. 13b,c).

After sunset, air over the land begins to cool, but air over the lake continues to warm in all cases, as the lake retains its heat for longer (Fig. 13). Although the timing differs slightly between cases, a land breeze H begins to form close to the eastern shoreline around 1900–2000 LT (Fig. 12). Consequently, the leading edge I of the lake breeze detaches from the main body (Fig. 12). Flow becomes offshore at 2100 LT during the dry period and DS storm and just after 1900 LT during the LR storm. In all cases, the prevailing southeasterlies surge westward and merge with the lake breeze.

Driven by the southeasterly flow, the convergence and associated upward motion propagate across the lake during the dry period and LR storm case studies (Figs. 12a,b, J). In the latter case, the leading edge of the storm propagates along with the convergence. The propagation speeds across the lake are $\sim 10 \text{ m s}^{-1}$ in the dry period and $\sim 6.5 \text{ m s}^{-1}$ during the LR storm (note this is also the storm propagation speed). Behind the convergence in the dry period, the wind speed rapidly increases to greater than 8 m s^{-1} , despite a lack of storm. The storm G over land during the DS storm case dissipates and does not propagate over the lake. The propagation of convergence J is blocked ~ 40 km offshore by the strong westerlies K across the lake (Fig. 12c), which occur due to the low θ_v air to west L (Fig. 13c). A new storm M forms along this land–breeze convergence over the lake around 0800 LT (Figs. 12c and 13c). In addition to the lake moisture source, additional moisture N is advected onto the lake from the land overnight to further fuel this storm (Fig. 13c).

During the dry period, the leading edge of the offshore flow advects the moist, high θ_v air accumulated on

the eastern shore back across the lake. To the east of the moisture and θ_v maximum O, which marks the center of the moist bulge described in section 3b, q and θ_v decrease as cool, dry air from the east is advected onto the lake by the land-breeze density current. However, there is no sharp decrease in these variables because the air moistens and warms as it moves across the lake. Over time, the horizontal extent of the moist bulge increases as the moisture gradient between the land and the lake weakens further, shown by the increased spacing of the specific humidity contours with time in Fig. 13a.

The LR storm F propagates continuously onto the lake from over land, although there is a temporary reduction in intensity as it crosses the eastern shore of the lake (narrowing of OLR contours across the 0 km dashed line in Figs. 12b and 13b). Once over the lake, the rear of the storm remains almost stationary and the storm grows at its leading edge. In contrast, the storms over the land and lake (G and M respectively) in the DS case arise from separate initiations (distinct minima in OLR contours over land and lake in Figs. 12c and 13c). The storm which forms over the lake during the morning shows little propagation, as the land breeze from the east is prevented from propagating across the lake by the anomalously strong land breeze K from the west (Fig. 12c).

4. Summary

Two case studies of storms over the Lake Victoria basin, and a further case of a dry period, were simulated using a convection-permitting configuration of the MetUM with 1.5 km horizontal grid spacing. This is the first time that the role—and interaction of—the large-scale conditions, lake–land-breeze circulation, and mountain flow in convergence and convection initiation/propagation over the Lake Victoria basin have been described and analyzed in such detail.

Key characteristics of each case study and their differences are summarized in Table 2 and the schematics in Fig. 14 (dry period) and Fig. 15 (LR and DS storms). In general, the large-scale circulation patterns are very similar between all three cases, as shown in Fig. 5; southeasterlies prevail across the region, except across Lake Victoria and to the northwest during the DS storm. The mean wind speed over the lowest 5 km does not vary much between cases, but is smallest during the dry period (5.1 m s^{-1} , compared with 5.7 and 5.5 m s^{-1} in the LR and DS storms respectively, first column, Table 2). However, the wind speed is actually greatest at the surface during the dry period (not shown). While the large-scale circulation is very similar between cases, Fig. 5 clearly shows large-scale differences in near-surface

moisture between the cases. Mean specific humidity in the lowest 5 km over the region is $\sim 3 \text{ g kg}^{-1}$ greater during the LR case study than the dry period case (fifth column, Table 2). Climatologically this is expected, as the mean monthly q is 1.1 g kg^{-1} higher in May compared to July (fourth column, Table 2). Specific humidity is greater during the DS storm case than the dry period case, since additional moisture is advected into the region from the Congo basin by the anomalous northwesterly wind. Table 2 (second and third columns) shows that mean potential temperature over the lowest 5 km does not change much between cases. However, the temperature in the DS storm case is lower than the dry period, likely because of the cold air associated with the storm to the northwest of the lake.

The LR storm initiates over land off the eastern shore of the lake during the afternoon, persists for ~ 21 h and has a lower mean OLR, whereas the DS storm initiates in the early morning over the lake itself, persists for about half as long and has a lower amount of cold, high cloud tops (8th, 9th, 10th, and 16th columns, Table 2). Mean accumulated rainfall over the storms' lifetime is much larger in the LR storm, when accumulations are averaged over the whole lake or just over the storm area (14th and 15th columns, Table 2). This is due to a combination of a larger storm area, longer storm duration and more intense rainfall rates.

Figures 14a,d and 15a,d show the strong similarities in the eastern lake breeze (blue arrows) and its evening convergence with the easterly prevailing winds, which are strengthened as they flow down the slopes of the Kenyan Highlands (red arrows), in the dry period and LR storm case studies. The reason that a storm forms along the convergence in the latter case is the moisture-laden air and high CAPE over land to the east of Lake Victoria, which allows deep convection to be triggered. Initiation is prevented in the dry period case by high CIN over the region. In both case studies, there is also subsequent overnight propagation of the convergence line over the lake as the easterly winds (including a land breeze and katabatic component) accelerate. The LR storm propagates along with the convergence line (Figs. 14b,c,e,f and 15b,c,e,f).

In the DS storm case, the surface winds across the lake are dominated by an anomalously strong land breeze from the northwest (Figs. 15g–i, purple arrows). This breeze originates from a region of particularly cool, moist air to the northwest of the lake (purple ellipses), remnants of an intense storm on the preceding day. Consequently, the overnight temperature gradient between the lake and land is strengthened in the northwest, forming a strong land breeze from this direction. The northwesterly land breeze converges with

TABLE 2. A comparison of various dynamic and thermodynamic variables and descriptive factors for the three case studies. Wind speeds, θ , and q are averaged over the lowest 5 km of the atmosphere above the region in Fig. 1b, and over a 24 h period from 1200 LT 10 Jul 2015, 6 May 2015, and 28 Jul 2016 for the dry period, LR storm, and DS storm, respectively. Where a monthly mean is shown, this is given by the ERA-Interim mean between 1997 and 2016. CAPE and CIN are the mean values from the region and times in Fig. 8, computed over lake/land grid points as indicated. CIN is only calculated where CAPE > 400 J kg⁻¹. Accumulated rainfall and mean OLR for the duration of the storm are computed over a box containing Lake Victoria and mean rainfall is also computed only over the storm area (where rainfall exceeds 0.1 mm h⁻¹). Other relevant factors are also noted.

Case	(1) Wind speed (m s ⁻¹) + direction	(2) θ (K) (ERA-Interim monthly mean)	(3) θ (K) (model 24 h mean)	(4) q (g kg ⁻¹) (ERA-Interim monthly mean)	(5) q (g kg ⁻¹) (model 24 h mean)	(6) CAPE/CIN over land at 1800 LT (J kg ⁻¹)	(7) CAPE/CIN over lake at 0600 LT (J kg ⁻¹)	(8) Location of storm initiation	(9) Time of storm initiation (LT)	(10) Storm duration	(11) Reason for low-level convergence	(12) Moisture source	(13) Mountain flow	(14) Accumulated rainfall over lake over storm life (mm)	(15) Accumulated rainfall over storm area over storm life (mm)	(16) Mean OLR over storm life (W m ⁻²)
Dry period	5.1 (SE)	314.5	316.0	5.9	4.9	CAPE: 140 CIN: 111	CAPE: 163 CIN: 21	Eastern shore of lake	—	—	Convergence between lake breeze and easterly prevailing winds	—	Downslope	—	—	—
LR storm	5.7 (SE)	315.6	315.8	7.0	7.8	CAPE: 318 CIN: 53	CAPE: 642 CIN: 18	Eastern shore of lake	1530	21	Convergence between lake breeze and easterly prevailing winds	Land initially, lake once storm is over lake	Downslope	14.3	95.5	217.1
DS storm	5.5 (SE, NW over lake)	314.5	314.9	5.9	6.1	CAPE: 226 CIN: 30	CAPE: 1051 CIN: 39	Center of lake	0530	10	Convergence between east and west land breezes. A particularly strong land breeze from the west is caused by cold air to the NW associated with convection from previous day	Lake and northwest	Downslope	1.17	41.3	251.1

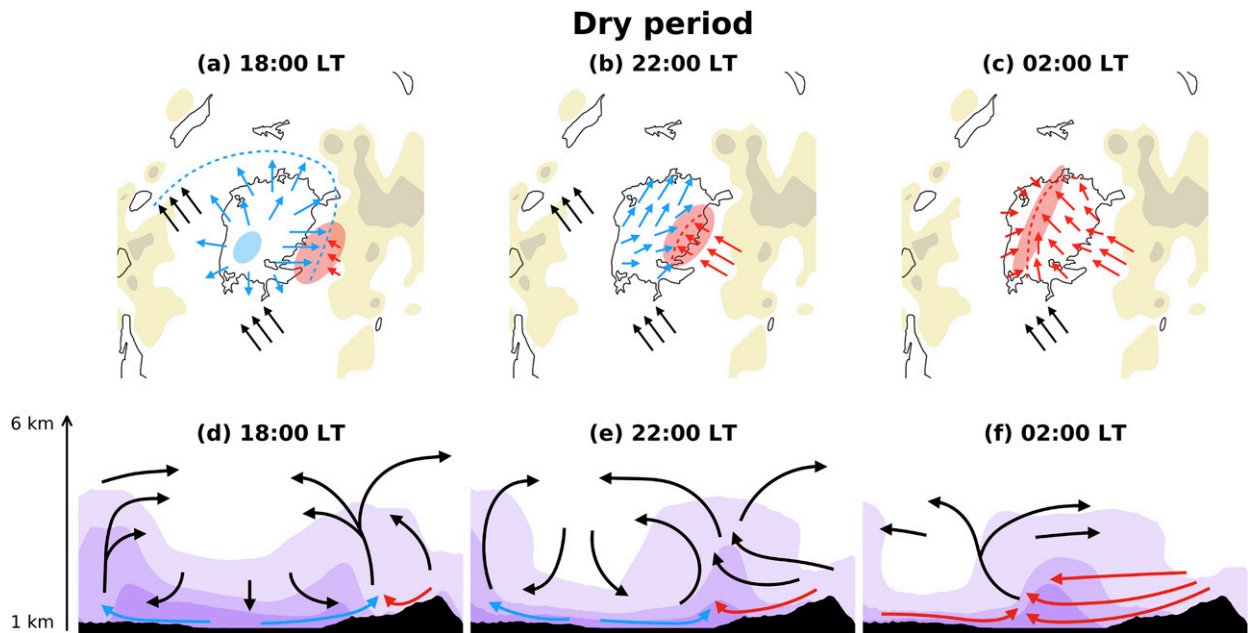


FIG. 14. Schematics showing maps and cross sections of the low-level wind, convergence, and moisture over Lake Victoria during the dry period case study. The blue dashed lines represent the lake-breeze front and the red dashed lines represent the leading edge of the offshore flow. Black arrows on the maps represent the prevailing wind, but represent the flow of air from mixed origins on the cross sections. Blue arrows represent lake breezes and red arrows represent offshore flow (encompassing land breezes, downslope flows, and prevailing winds). Blue and red ellipses represent areas of strong divergence and convergence, respectively. Purple contours on the cross sections show specific humidity.

the offshore flow from the east (red arrows) over the center of the lake at 0600 LT and causes a bulge of moist air over the center of the lake (Figs. 15h,k). High CAPE over the lake results in deep convection. Westward propagation of the convergence line (and storm) across the lake is blocked by the strong northwesterlies.

The moisture to initiate the LR storm originates mainly over land, but the moisture source changes to lake BL air once the storm propagates over the lake (black arrows, purple contours, Figs. 15d–f). In contrast, moist lake BL air is predominantly responsible for the initiation of the DS storm, with the advection of additional moisture onto the lake from the northwest (purple arrows and contours, Figs. 15k,l).

5. Discussion and conclusions

The lake–land-breeze circulation was shown to be the major control on the initiation location, timing and propagation of convection over the Lake Victoria basin, affirming its importance for forecasting convection in this region. Many aspects of the case studies—in particular the diurnal cycle in convergence and divergence over Lake Victoria—agree with the mean picture described by Mukabana and Piekle (1996), Ba and Nicholson (1998), Song et al. (2004), Anyah et al. (2006),

Thiery et al. (2015), and Camberlin et al. (2018). However, the differences between the cases demonstrate the importance of daily to seasonal variability in local winds and large-scale moisture availability in storm initiation and propagation, and show that individual storms cannot be understood using the mean diurnal cycle alone.

The lake–land-breeze circulations were remarkably similar during the dry period and LR case study. A moist and high-CAPE/low-CIN atmosphere was shown to be the important factor for triggering a storm in the LR case. The additional moisture was shown to be, at least in part, a seasonal effect. However, moisture content may also vary locally on subseasonal time scales.

The LR storm forms over land to the east of Lake Victoria and subsequently propagates onto the lake. Camberlin et al. (2018) used a mean diurnal cycle of satellite observations to suggest that such a propagation may occur. However, their study was not conclusive as to whether the mean rainfall over the land and lake result from the same storms, due to a discontinuity in propagation speeds over the Kenyan Highlands (slower) and lake (faster). The LR case shows that continuous propagation from land to lake may indeed occur with a discontinuity between phase speeds over the different surfaces; the evening convection to the east of the lake is

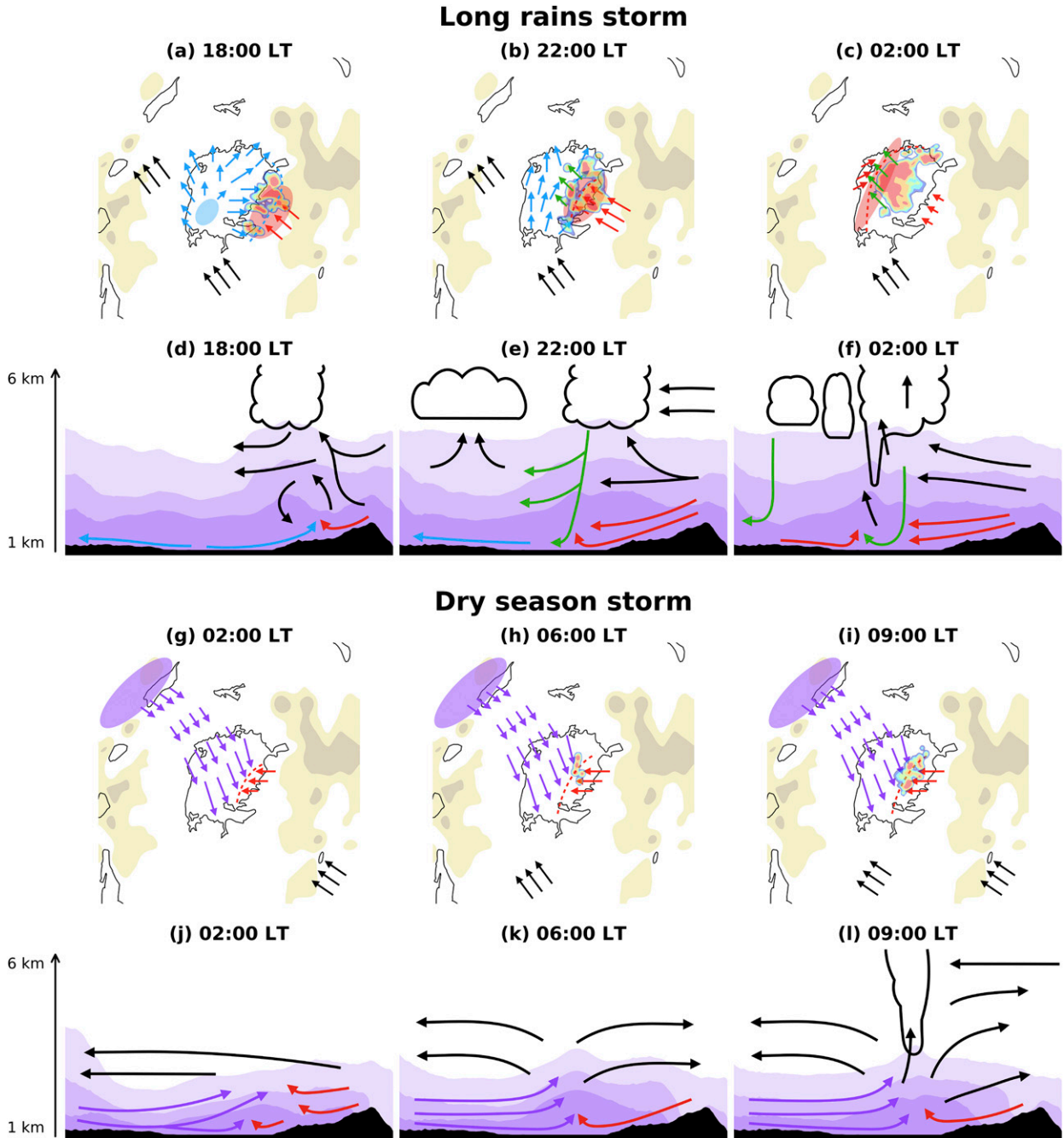


FIG. 15. Schematics showing maps and cross sections of the low-level wind, convergence, and moisture over Lake Victoria during the LR and DS storm case studies. Symbols as in Fig. 14. Green arrows represent storm outflow and purple arrows represent the anomalously strong land breeze from the northwest. Purple ellipses represent regions of cool, moist air. The smoothed precipitation field is also plotted on the maps.

effectively stalled until it moves onto the lake overnight, after which its propagation speed increases.

The DS storm demonstrates the importance of convection from the previous day in altering the local atmosphere—in this case a long-lived cold pool to the northwest of the lake strengthening the land breeze

from the west—and creating an environment conducive to storms over the lake. This result supports a study by Thiery et al. (2016), which noted a strong correlation between intense storms over land during the afternoon and intense nocturnal storms over Lake Victoria, and in part attributed this to long-lived cold

pools. Thiery et al. (2017) used this correlation in a statistical storm predictor [Lake Victoria Intense Early Warning System (VIEWS)] for short-range forecasting. For longer-range forecasts, skill could be enhanced by improving cold pool simulation in dynamical models.

Analysis of the two dry season cases has highlighted the formation of a bulge of moist air above the convergence at the surface of Lake Victoria. Such a feature has not been described in previous literature on collisions of density currents, partly because few studies focus on collisions over a water body, and partly because humidity is neglected in such studies. In the DS storm case, CAPE is high and CIN is low, so a storm is initiated above the moist bulge. There is no clear moist bulge during the LR storm, likely because there is less contrast in specific humidity between air near the surface over the lake and land and because strong circulations associated with the storms may disrupt its development.

Birch and Reeder (2013) and Birch et al. (2014) showed that the collision of offshore flow with a sea breeze can result in waves being excited and traveling upstream. Studies of density current collisions over land also show the excitation of waves (Kingsmill and Crook 2003; Goler and Reeder 2004). While no such waves were diagnosed in this study (the model data hourly time resolution was insufficient), it should not be ruled out that such waves may exist and may be responsible for upstream triggering of convection in some conditions.

During the dry period, sudden strong winds were associated with density current propagation from the east, despite the lack of storm. This suggests that the lake could pose a hazard to fishermen, even on a dry day. In general, the westward offshore propagation requires further study to elucidate the relative strengths of the land breeze, downslope flow and prevailing winds, to better understand the moisture bulge and assess potential hazards.

It is acknowledged that the conclusions drawn in this study are based solely on model simulations. This is due to the lack of high-resolution observations, in particular of low-level wind and moisture fields in this region. Moreover, the case studies presented here show just two examples of storms which occurred over the Lake Victoria basin, and their representativeness is unknown. In particular, it is acknowledged that the large-scale circulation pattern does not differ much between cases, and so its effect cannot be investigated in this study.

Given the very different characteristics of the two storms—and their correspondingly different triggers—it is very likely that other storm types and triggers also exist. It would be a natural extension of this work to classify storms over the lake—for example based on their time and location of initiation—and identify corresponding triggers in the local- and large-scale atmosphere. That

the storms analyzed in this study occurred in different seasons raises the question as to whether certain storm types and triggers are more likely in a given season.

Understanding the key processes involved in storm formation and propagation is necessary to assess their representation in forecast models, and therefore understand model behavior and make improvements where necessary. Ultimately, improved forecasts will lead to increased safety and reduced deaths on the lake.

Acknowledgments. This work was supported by the NERC SPHERES DTP (Grant NE/L002574/1). Woodhams was the grateful recipient of the Australian Bicentennial Award from the Menzies Centre at King's College London and the Rupert Ford Award from the Royal Meteorological Society to fund travel to the University of Melbourne. Marsham was also funded by the HyCRISTAL project (Grant NE/M02038X/1) and the NCAS ACREW project. Lane is supported by the Australian Research Council's Centres of Excellence Scheme (CE170100023). This work was also supported by U.K. Research and Innovation as part of the Global Challenges Research Fund, Grant NE/P021077/1 (GCRF African SWIFT). This project used the MetPy package developed by UCAR/Unidata (Unidata 2018). The GPM IMERG data were provided by the NASA Goddard Space Flight Center's Precipitation Measurement Missions Science Team and Precipitation Processing System, which develop and compute the GPM IMERG as a contribution to GPM, including data archiving at the NASA GES DISC. Brightness temperature data were provided by EUMETSAT and distributed by the SATMOS service (Météo-France/Center de Meteorologie Spatiale). We thank the ICARE Data and Services Center for providing access to this data. The authors thank Alexander Roberts for regridding the brightness temperature data and Martin Jucker for code to compute model level heights. The authors would also like to thank the anonymous reviewers for improving the quality and clarity of the paper.

REFERENCES

- Albrecht, R. I., S. J. Goodman, D. E. Buechler, R. J. Blakeslee, and H. J. Christian, 2016: Where are the lightning hotspots on Earth? *Bull. Amer. Meteor. Soc.*, **97**, 2051–2068, <https://doi.org/10.1175/BAMS-D-14-00193.1>.
- Anyah, R. O., F. H. Semazzi, and L. Xie, 2006: Simulated physical mechanisms associated with climate variability over Lake Victoria Basin in East Africa. *Mon. Wea. Rev.*, **134**, 3588–3609, <https://doi.org/10.1175/MWR3266.1>.
- Aranami, K., T. Davies, and N. Wood, 2015: A mass restoration scheme for limited-area models with semi-Lagrangian advection. *Quart. J. Roy. Meteor. Soc.*, **141**, 1795–1803, <https://doi.org/10.1002/qj.2482>.

- Ba, M. B., and S. E. Nicholson, 1998: Analysis of convective activity and its relationship to the rainfall over the Rift Valley lakes of East Africa during 1983–90 using the Meteosat infrared channel. *J. Appl. Meteor.*, **37**, 1250–1264, [https://doi.org/10.1175/1520-0450\(1998\)037<1250:AOCAL>2.0.CO;2](https://doi.org/10.1175/1520-0450(1998)037<1250:AOCAL>2.0.CO;2).
- Ballentine, R. J., 1982: Numerical simulation of land-breeze-induced snowbands along the western shore of Lake Michigan. *Mon. Wea. Rev.*, **110**, 1544–1553, [https://doi.org/10.1175/1520-0493\(1982\)110<1544:NSOLBI>2.0.CO;2](https://doi.org/10.1175/1520-0493(1982)110<1544:NSOLBI>2.0.CO;2).
- Birch, C. E., and M. J. Reeder, 2013: Wave-cloud lines over northwest Australia. *Quart. J. Roy. Meteor. Soc.*, **139**, 1311–1326, <https://doi.org/10.1002/qj.2043>.
- , —, and G. Berry, 2014: Wave-cloud lines over the Arabian Sea. *J. Geophys. Res. Atmos.*, **119**, 4447–4457, <https://doi.org/10.1002/2013JD021347>.
- , M. J. Roberts, L. Garcia-Carreras, D. Ackerley, M. J. Reeder, A. P. Lock, and R. Schiemann, 2015: Sea-breeze dynamics and convection initiation: The influence of convective parameterization in weather and climate model biases. *J. Climate*, **28**, 8093–8108, <https://doi.org/10.1175/JCLI-D-14-00850.1>.
- Camberlin, P., W. Gitau, O. Planchon, V. Dubreuil, B. M. Funatsu, and N. Philippon, 2018: Major role of water bodies on diurnal precipitation regimes in Eastern Africa. *Int. J. Climatol.*, **38**, 613–629, <https://doi.org/10.1002/joc.5197>.
- Cannon, T., F. Krüger, G. Bankoff, and L. Schipper, 2014: Putting culture at the centre of risk reduction. *World Disasters Report 2014: Focus on Culture and Risk*, T. Cannon and L. Schipper, Eds., International Federation of Red Cross and Red Crescent Societies, 185–209.
- Chamberlain, J., C. Bain, D. Boyd, K. McCourt, T. Butcher, and S. Palmer, 2014: Forecasting storms over Lake Victoria using a high resolution model. *Meteor. Appl.*, **21**, 419–430, <https://doi.org/10.1002/met.1403>.
- Datta, R., 1981: Certain aspects of monsoonal precipitation dynamics over Lake Victoria. *Monsoon Dynamics*, J. Lighthill and R. Pearce, Eds., Cambridge University Press, 333–349.
- Dee, D. P., and Coauthors, 2011: The ERA-Interim reanalysis: Configuration and performance of the data assimilation system. *Quart. J. Roy. Meteor. Soc.*, **137**, 553–597, <https://doi.org/10.1002/qj.828>.
- EUMETSAT, 2012: The conversion from effective radiances to equivalent brightness temperatures. EUM/MET/TEN/11/0569. v1. Tech. Rep., EUMETSAT, 49 pp.
- Fiedler, E. K., M. J. Martin, and J. Roberts-Jones, 2014: An operational analysis of lake surface water temperature. *Tellus*, **66A**, 21247, <https://doi.org/10.3402/tellusa.v66.21247>.
- Finney, D. L., and Coauthors, 2019: Implications of improved representation of convection for the East Africa water budget using a convection-permitting model. *J. Climate*, **32**, 2109–2129, <https://doi.org/10.1175/JCLI-D-18-0387.1>.
- Flohn, H., and K. Fraedrich, 1966: Tagesperiodische zirkulation und niederschlagsverteilung am Victoria-See (Ostafrika) (The daily periodic circulation and distribution of rainfall over Lake Victoria, in German). *Meteor. Rundsch.*, **19** (6), 157–165.
- , and T. Burkhardt, 1985: Nile runoff at Aswan and Lake Victoria: A case of a discontinuous climate time series. *Z. Gletscherk. Glazialgeol.*, **21**, 125–130.
- Fraedrich, K., 1972: A simple climatological model of the dynamics and energetics of the nocturnal circulation at Lake Victoria. *Quart. J. Roy. Meteor. Soc.*, **98**, 322–335, <https://doi.org/10.1002/qj.49709841606>.
- Goler, R. A., and M. J. Reeder, 2004: The generation of the morning glory. *J. Atmos. Sci.*, **61**, 1360–1376, [https://doi.org/10.1175/1520-0469\(2004\)061<1360:TGOTMG>2.0.CO;2](https://doi.org/10.1175/1520-0469(2004)061<1360:TGOTMG>2.0.CO;2).
- Gregory, D., and P. Rowntree, 1990: A mass flux convection scheme with representation of cloud ensemble characteristics and stability-dependent closure. *Mon. Wea. Rev.*, **118**, 1483–1506, [https://doi.org/10.1175/1520-0493\(1990\)118<1483:AMFCSW>2.0.CO;2](https://doi.org/10.1175/1520-0493(1990)118<1483:AMFCSW>2.0.CO;2).
- Hastings, D. A., and P. K. Dunbar, 1999: Global Land One-kilometer Base Elevation (GLOBE) digital elevation model, documentation, volume 1.0. Key to Geophysical Records Documentation (KGRD), Doc. 34, National Oceanic and Atmospheric Administration, National Geophysical Data Center, <https://repository.library.noaa.gov/view/noaa/13424>.
- Hjelmfelt, M. R., and R. R. Braham Jr., 1983: Numerical simulation of the airflow over Lake Michigan for a major lake-effect snow event. *Mon. Wea. Rev.*, **111**, 205–219, [https://doi.org/10.1175/1520-0493\(1983\)111<0205:NSOTAO>2.0.CO;2](https://doi.org/10.1175/1520-0493(1983)111<0205:NSOTAO>2.0.CO;2).
- Hong, Y., K.-L. Hsu, S. Sorooshian, and X. Gao, 2004: Precipitation estimation from remotely sensed imagery using an artificial neural network cloud classification system. *J. Appl. Meteor. Climatol.*, **43**, 1834–1853, <https://doi.org/10.1175/JAM2173.1>.
- Hou, A. Y., and Coauthors, 2014: The Global Precipitation Measurement Mission. *Bull. Amer. Meteor. Soc.*, **95**, 701–722, <https://doi.org/10.1175/BAMS-D-13-00164.1>.
- Huffman, G. J., 2017: GPM IMERG Final Precipitation L3 Half Hourly 0.1 degree \times 0.1 degree V05. Goddard Earth Sciences Data and Information Services Center (GES DISC), Greenbelt, MD, accessed 20 December 2017, <https://doi.org/10.5067/GPM/IMERG/3B-HH/05>.
- , and Coauthors, 2007: The TRMM Multisatellite Precipitation Analysis (TMPA): Quasi-global, multiyear, combined-sensor precipitation estimates at fine scales. *J. Hydrometeorol.*, **8**, 38–55, <https://doi.org/10.1175/JHM560.1>.
- , and Coauthors, 2018: Algorithm Theoretical Basis Document (ATBD), version 5.2. NASA Global Precipitation Measurement (GPM) Integrated Multi-satellite Retrievals for GPM (IMERG). Tech. Rep., 35 pp., https://pmm.nasa.gov/sites/default/files/document_files/IMERG_ATBD_V5.2.pdf.
- Joyce, R. J., and P. Xie, 2011: Kalman filter-based CMORPH. *J. Hydrometeorol.*, **12**, 1547–1563, <https://doi.org/10.1175/JHM-D-11-022.1>.
- , J. E. Janowiak, P. A. Arkin, and P. Xie, 2004: CMORPH: A method that produces global precipitation estimates from passive microwave and infrared data at high spatial and temporal resolution. *J. Hydrometeorol.*, **5**, 487–503, [https://doi.org/10.1175/1525-7541\(2004\)005<0487:CAMTPG>2.0.CO;2](https://doi.org/10.1175/1525-7541(2004)005<0487:CAMTPG>2.0.CO;2).
- Keen, C. S., and W. A. Lyons, 1978: Lake/land breeze circulations on the western shore of Lake Michigan. *J. Appl. Meteor.*, **17**, 1843–1855, [https://doi.org/10.1175/1520-0450\(1978\)017<1843:LBCOTW>2.0.CO;2](https://doi.org/10.1175/1520-0450(1978)017<1843:LBCOTW>2.0.CO;2).
- Kendon, E. J., N. M. Roberts, C. A. Senior, and M. J. Roberts, 2012: Realism of rainfall in a very high-resolution regional climate model. *J. Climate*, **25**, 5791–5806, <https://doi.org/10.1175/JCLI-D-11-00562.1>.
- Kim, K., J. Park, J. Baik, and M. Choi, 2017: Evaluation of topographical and seasonal feature using GPM IMERG and TRMM 3B42 over Far-East Asia. *Atmos. Res.*, **187**, 95–105, <https://doi.org/10.1016/j.atmosres.2016.12.007>.
- Kingsmill, D. E., and A. N. Crook, 2003: An observational study of atmospheric bore formation from colliding density currents. *Mon. Wea. Rev.*, **131**, 2985–3002, [https://doi.org/10.1175/1520-0493\(2003\)131<2985:AOSOAB>2.0.CO;2](https://doi.org/10.1175/1520-0493(2003)131<2985:AOSOAB>2.0.CO;2).
- Lean, H. W., P. A. Clark, M. Dixon, N. M. Roberts, A. Fitch, R. Forbes, and C. Halliwell, 2008: Characteristics of high-resolution versions

- of the Met Office Unified Model for forecasting convection over the United Kingdom. *Mon. Wea. Rev.*, **136**, 3408–3424, <https://doi.org/10.1175/2008MWR2332.1>.
- Lumb, F., 1970: Topographic influences on thunderstorm activity near Lake Victoria. *Weather*, **25**, 404–410, <https://doi.org/10.1002/j.1477-8696.1970.tb04129.x>.
- Lyons, W. A., 1972: The climatology and prediction of the Chicago lake breeze. *J. Appl. Meteor.*, **11**, 1259–1270, [https://doi.org/10.1175/1520-0450\(1972\)011<1259:TCAPOT>2.0.CO;2](https://doi.org/10.1175/1520-0450(1972)011<1259:TCAPOT>2.0.CO;2).
- , and L. E. Olsson, 1972: Mesoscale air pollution transport in the Chicago lake breeze. *J. Air Pollut. Control Assoc.*, **22**, 876–881, <https://doi.org/10.1080/00022470.1972.10469725>.
- Marsham, J. H., N. S. Dixon, L. Garcia-Carreras, G. Lister, D. J. Parker, P. Knippertz, and C. E. Birch, 2013: The role of moist convection in the West African monsoon system: Insights from continental-scale convection-permitting simulations. *Geophys. Res. Lett.*, **40**, 1843–1849, <https://doi.org/10.1002/grl.50347>.
- Mukabana, J. R., and R. A. Pielke, 1996: Investigating the influence of synoptic-scale monsoonal winds and mesoscale circulations on diurnal weather patterns over Kenya using a mesoscale numerical model. *Mon. Wea. Rev.*, **124**, 224–244, [https://doi.org/10.1175/1520-0493\(1996\)124<0224:ITIOSS>2.0.CO;2](https://doi.org/10.1175/1520-0493(1996)124<0224:ITIOSS>2.0.CO;2).
- Nicholson, S., 1996: A review of climate dynamics and climate variability in Eastern Africa. *The Limnology, Climatology and Paleoclimatology of the East African Lakes*, T. C. Johnson and E. O. Odada, Eds., Gordon and Breach Publishers, 25–56.
- , and X. Yin, 2002: Mesoscale patterns of rainfall, cloudiness and evaporation over the great lakes of East Africa. *The East African Great Lakes: Limnology, Palaeolimnology and Biodiversity*, E. O. Odada and D. O. Olago, Eds., Kluwer Academic Publishers, 93–120.
- Okeyo, A. E., 1986: The impact of Lake Victoria on the convective activities over the Kenya Highlands. *J. Meteor. Soc. Japan*, **64**, 689–695.
- Passarelli, R. E., Jr., and R. R. Brahm Jr., 1981: The role of the winter land breeze in the formation of Great Lake snow storms. *Bull. Amer. Meteor. Soc.*, **62**, 482–491, [https://doi.org/10.1175/1520-0477\(1981\)062<0482:TROTWL>2.0.CO;2](https://doi.org/10.1175/1520-0477(1981)062<0482:TROTWL>2.0.CO;2).
- Schmetz, J., P. Pili, S. Tjemkes, D. Just, J. Kerkmann, S. Rota, and A. Ratier, 2002: An introduction to Meteosat Second Generation (MSG). *Bull. Amer. Meteor. Soc.*, **83**, 977–992, [https://doi.org/10.1175/1520-0477\(2002\)083<0977:AITMSG>2.3.CO;2](https://doi.org/10.1175/1520-0477(2002)083<0977:AITMSG>2.3.CO;2).
- Schneider, U., A. Becker, A. Meyer-Christoffer, M. Ziese, and B. Rudolf, 2008: Global precipitation analysis products of the GPCP. Tech. Rep., Deutscher Wetterdienst, 12 pp., ftp://ds1.iap.ac.cn/ftp/ds088_GPCP5-full_0.5_1month_ascii/GPCP_intro_products_2008.pdf.
- Semazzi, F., 2011: Enhancing safety of navigation and efficient exploitation of natural resources over Lake Victoria and its basin by strengthening meteorological services on the lake. Tech. Rep., North Carolina State University Climate Modeling Laboratory, 104 pp.
- Sills, D., J. Brook, I. Levy, P. Makar, J. Zhang, and P. Taylor, 2011: Lake breezes in the southern Great Lakes region and their influence during BAQS-Met 2007. *Atmos. Chem. Phys.*, **11**, 7955–7973, <https://doi.org/10.5194/acp-11-7955-2011>.
- Song, Y., F. H. Semazzi, L. Xie, and L. J. Ogallo, 2004: A coupled regional climate model for the Lake Victoria basin of East Africa. *Int. J. Climatol.*, **24**, 57–75, <https://doi.org/10.1002/joc.983>.
- Sorooshian, S., K.-L. Hsu, X. Gao, H. V. Gupta, B. Imam, and D. Braithwaite, 2000: Evaluation of PERSIANN system satellite-based estimates of tropical rainfall. *Bull. Amer. Meteor. Soc.*, **81**, 2035–2046, [https://doi.org/10.1175/1520-0477\(2000\)081<2035:EOPSS>2.3.CO;2](https://doi.org/10.1175/1520-0477(2000)081<2035:EOPSS>2.3.CO;2).
- Stratton, R. A., and Coauthors, 2018: A Pan-African Convection-Permitting Regional Climate Simulation with the Met Office Unified Model: CP4-Africa. *J. Climate*, **31**, 3485–3508, <https://doi.org/10.1175/JCLI-D-17-0503.1>.
- Sungmin, O., and P.-E. Kirstetter, 2018: Evaluation of diurnal variation of GPM IMERG-derived summer precipitation over the contiguous US using MRMS data. *Quart. J. Roy. Meteor. Soc.*, **144**, 270–281, <https://doi.org/10.1002/qj.3218>.
- , U. Foelsche, G. Kirchengast, J. Fuchsberger, T. Jackson, and W. A. Petersen, 2017: Evaluation of GPM IMERG early, late, and final rainfall estimates using WegenerNet gauge data in southeastern Austria. *Hydrol. Earth Syst. Sci.*, **21**, 6559–6572, <https://doi.org/10.5194/hess-21-6559-2017>.
- Tang, G., Y. Ma, D. Long, L. Zhong, and Y. Hong, 2016: Evaluation of GPM Day-1 IMERG and TMPA Version-7 legacy products over Mainland China at multiple spatiotemporal scales. *J. Hydrol.*, **533**, 152–167, <https://doi.org/10.1016/j.jhydrol.2015.12.008>.
- Tang, Y., H. W. Lean, and J. Bornemann, 2013: The benefits of the Met Office variable resolution NWP model for forecasting convection. *Meteor. Appl.*, **20**, 417–426, <https://doi.org/10.1002/met.1300>.
- Thiery, W., E. L. Davin, H.-J. Panitz, M. Demuzere, S. Lhermitte, and N. Van Lipzig, 2015: The impact of the African Great Lakes on the regional climate. *J. Climate*, **28**, 4061–4085, <https://doi.org/10.1175/JCLI-D-14-00565.1>.
- , —, S. I. Seneviratne, K. Bedka, S. Lhermitte, and N. P. van Lipzig, 2016: Hazardous thunderstorm intensification over Lake Victoria. *Nat. Commun.*, **7**, 12786, <https://doi.org/10.1038/ncomms12786>.
- , L. Gudmundsson, K. Bedka, F. H. Semazzi, S. Lhermitte, P. Willems, N. P. van Lipzig, and S. I. Seneviratne, 2017: Early warnings of hazardous thunderstorms over Lake Victoria. *Environ. Res. Lett.*, **12**, 074012, <https://doi.org/10.1088/1748-9326/aa7521>.
- Unidata, 2018: MetPy: A Python Package for Meteorological Data, version 0.4.3. UCAR/Unidata, Boulder, CO, accessed 15 March 2019, <https://doi.org/10.5065/D6WW7G29>.
- Virts, K. S., J. M. Wallace, M. L. Hutchins, and R. H. Holzworth, 2013: Highlights of a new ground-based, hourly global lightning climatology. *Bull. Amer. Meteor. Soc.*, **94**, 1381–1391, <https://doi.org/10.1175/BAMS-D-12-00082.1>.
- Wang, R., J. Chen, and X. Wang, 2017: Comparison of IMERG Level-3 and TMPA 3B42V7 in estimating typhoon-related heavy rain. *Water*, **9** (4), 276, <https://doi.org/10.3390/w9040276>.
- Wood, N., and Coauthors, 2014: An inherently mass-conserving semi-implicit semi-Lagrangian discretization of the deep-atmosphere global non-hydrostatic equations. *Quart. J. Roy. Meteor. Soc.*, **140**, 1505–1520, <https://doi.org/10.1002/qj.2235>.
- Woodhams, B., C. E. Birch, J. Marsham, C. Bain, N. Roberts, and D. Boyd, 2018: What is the added value of a convection-permitting model for forecasting extreme rainfall over tropical East Africa? *Mon. Wea. Rev.*, **146**, 2757–2780, <https://doi.org/10.1175/MWR-D-17-0396.1>.
- Xu, R., F. Tian, L. Yang, H. Hu, H. Lu, and A. Hou, 2017: Ground validation of GPM IMERG and TRMM 3B42V7 rainfall products over southern Tibetan Plateau based on a high-density rain gauge network. *J. Geophys. Res. Atmos.*, **122**, 910–924, <https://doi.org/10.1002/2016JD025418>.
- Yin, X., S. E. Nicholson, and M. B. Ba, 2000: On the diurnal cycle of cloudiness over Lake Victoria and its influence on evaporation from the lake. *Hydrol. Sci. J.*, **45**, 407–424, <https://doi.org/10.1080/02626660009492338>.